Lawrence Berkeley National Laboratory
LBL Publications

Title

Temporal evolution of soil moisture statistical fractal and controls by soil texture and regional groundwater flow

Permalink

Authors

Ji, Xinye
Shen, Chaopeng
Riley, William J

Publication Date

DOI

Peer reviewed

Temporal evolution of soil moisture statistical fractal and controls by soil texture and regional groundwater flow

[XinyeJi](#)[a], [Chaopeng Shen](#)[a], [William J. Riley](#)[b]

a Department of Civil and Environmental Engineering, The Pennsylvania State University, University Park, PA 16802, USA
b Earth Science Division, Lawrence Berkeley National Lab, Berkeley, CA 94720, USA

Highlights

- Soil moisture statistical fractal temporal evolution shows seasonal trends and a three-phase event-induced hysteretic patterns.
- Soil texture is the main cause of hysteresis in fractal temporal evolution; groundwater has important influences that interact with other factors.
- We separated out the effects of different controls and generalized phenomenological rules that govern fractal evolution.

Abstract

Soil moisture statistical fractal is an important tool for downscaling remotely-sensed observations and has the potential to play a key role in multi-scale hydrologic modeling. The fractal was first introduced two decades ago, but relatively little is known regarding how its scaling exponents evolve in time in response to climatic forcings. Previous studies have neglected the process of moisture re-distribution due to regional groundwater flow. In this study we used a physically-based surface-subsurface processes model and numerical experiments to elucidate the patterns and controls of fractal temporal evolution in two U.S. Midwest basins. Groundwater flow was found to introduce large-scale spatial structure, thereby reducing the scaling exponents (τ), which has implications for the transferability of calibrated parameters to predict τ. However, the groundwater effects depend on complex interactions with other physical controls such as soil texture and land use. The fractal scaling exponents, while in general showing a seasonal mode that correlates with mean moisture content, display hysteresis after storm events that can be divided into three phases, consistent with literature findings: (a) wetting, (b) re-organizing, and (c) dry-down. Modeling experiments clearly show that the hysteresis is attributed to soil texture, whose "patchiness" is the primary contributing factor. We generalized phenomenological rules for the impacts of rainfall, soil texture, groundwater flow, and land use on τ evolution. Grid resolution has a mild influence on the results and there is a strong correlation between predictions of τ from different resolutions. Overall, our results suggest that groundwater flow should be given more consideration in studies of the soil moisture statistical fractal, especially in regions with a shallow water table.

1. Introduction

Spatial and temporal variations in soil moisture strongly affect many hydrologic processes, including infiltration, evapotranspiration (ET), and subsurface flow [1], [2], [3], [4], [5], [6], [7], [8]. Downscaling (inferring fine-scale spatial distribution from coarse-resolution data) soil moisture can help improve the accuracy of modeling these nonlinear,

moisture-dependent processes [9], [10], [11]. Spatial scaling laws are useful tools for downscaling coarse-grained remotely-sensed observations [12], [13], [14], [15], [16].

Current techniques for the soil moisture downscaling problem include model-based disaggregation [17], Empirical Orthogonal Function [18], Proper Orthogonal Decomposition Mapping Method [10] and multi-fractal-based approaches [19], [20], with which our work is primarily concerned. Since the seminal paper by Rodriguez-Iturbe et al. [21], it has been widely known that statistical moments of observed soil moisture exhibit power-law decay (e.g., see [11], [12], [19], [22], [23], [24], [25], [26], [27], [28]), which resembles a self-similar structure, or fractal, in a statistical sense (for a brief introduction, see Section 2.1). Previous modeling results [23], [29], [30] also show similar scaling relationships. These scale-invariant relationships and the associated scaling exponents may hold the key to enable estimation of subgrid-scale states from large scale dynamics for modeling purposes [14], [31].

In addition to providing a tool for observation-based downscaling, the statistical fractal may also contribute to solving the spatial scaling issue in hydrologic modeling. Hydrologic spatial scaling and heterogeneity have for decades been recognized as among the most significant challenges in hydrologic modeling [32]. Scaling problems arise when the models and their associated governing equations are applied at inappropriate spatial scales [33], leading to identifiability (or equifinality) problems [34] for scale-dependent hydrologic models [14], [35], [36], [37], [38]. Despite the importance of this problem, there is a lack of generalized subgrid scale integration theory. It has been common in other disciplines, e.g., soil structure [39], reactive transport [40], [41], modeling of orographic precipitation [42], geomechanics [43], etc., to employ scale-invariant relationships to infer fine-scale distributions with macro-scale data (e.g., [44], [45], [46]). However, we are not aware of the applications of scale-invariance in land surface hydrologic modeling.

Despite the potential usefulness of the soil moisture statistical fractal (SMSF), there is limited knowledge of how it evolves in time as watersheds undergo seasonal and daily climatic forcing. Although it is generally understood that a more 'patchy', disconnected, or 'wet islands' pattern has higher spatial 'intermittency' [20], [21], leading to higher scaling exponents, no quantitative or qualitative descriptions exist for the continuous temporal evolution of the SMSF, except for its relationships with mean moisture [25], [30]. There is even less understanding of the abiotic and biotic controls of the SMSF. Mascaro et al. [20] used mean moisture and calibrated parameters representing soil texture and vegetation as predictors for the SMSF scaling exponents, but did not examine the impacts of regional groundwater flow. In more humid regions, since groundwater flow likely produces hillslope-scale spatial soil moisture structure [47], we expect groundwater dynamics to exert controls on the SMSF scaling exponents. Whether the mean-moisture-driven formula proposed by Mascaro et al. [20] works for different geologic and groundwater flow settings is therefore worth investigation. Since an analytical formulation of SMSF scaling exponent evolution considering groundwater flow is not available, empirical evidence can be collected to synthesize patterns and phenomenological laws. Recent discussions encouraged the identification and use of patterns, emergent behaviors, and organizing principles to reduce the dimensionality of the prediction problem [48], [49], [50], [51], [52], [53].

The goals of this paper are two-fold: (1) to test the hypothesis that in humid regions, lateral groundwater flow can exert short- and long-term controls on the temporal evolution of the SMSF scaling exponents, comparable to the effects of soil texture, on the 10^{-2}–10^1 km^2 scale. More specifically, groundwater flow maintains spatial soil moisture structure and thus reduces the values of the SMSF scaling exponents; and (2) to identify and understand how SMSF scaling exponents evolve in response to seasonal and storm-event forcings. The span of spatial scales studied here is chosen because it fills the gap between regional climate modeling and physically-based hydrologic modeling scales, and is therefore of interest to future multi-scale modeling. We analyze the temporal evolution of the SMSF scaling exponents using a tested, physically-based, surface-subsurface processes model applied in two temperate watersheds. We focus on "deep why" explanations of the temporal dynamics and, ultimately, methods for representing heterogeneity in numerical models.

In the following, we first provide basic background of the soil moisture statistical multi-fractal. Then we present the impact of groundwater flow on fractal evolution by comparing simulations with and without lateral groundwater flow. Subsequently, we synthesize the temporal evolution patterns of the scaling exponents, explain their responses to seasonal and event forcings, and analyze their controls by soil texture, groundwater flow, and land use. Finally, we show results from different resolutions, as well as a different basin, and discuss the potential for application of the SMSF in large-scale models.

2. Methods

2.1. Multi-fractal analysis

We denote by $\theta(\lambda)$ the depth-averaged soil moisture (or, more generally, any spatially-distributed variable) in an observation window of size (support scale) $\lambda \times \lambda$ in a domain of size $L \times L$. The qth order central moment of $\theta(\lambda)$, $Sq(\lambda)$, is calculated as

$$S^q(\lambda) = \overline{\left[\theta(\lambda) - \overline{\theta(\lambda)}\right]^q} \tag{1}$$

where the average operator is taken over the specified domain of size $L \times L$. As discovered from both field observations and numerical simulations, increasing the support scale λ at steady state often leads to an approximate power-law decay of Sq:

$$S^q(\lambda) \propto \lambda^{-\tau(q)} \tag{2}$$

where $\tau(q)$ are the scaling exponents for each moment. Since the relationship is scale-invariant and self-similar, i.e.,

$\tau(q) \propto -\dfrac{\log(S^q(\lambda))}{\log(\lambda)}$ is a constant for all λ (within the λ bounds where this relationship holds), the field is fractal in a statistical sense when $0 < \tau(q) < 2$. At the bounds, $\tau(q) = 2$ corresponds to a completely uncorrelated random field, or white noise, and $\tau(q) = 0$ corresponds to a homogeneous field. When $\tau(q) \propto q$, the field is called monofractal and when $\tau(q)$ is a nonlinear function of q, the field is called multifractal. $\tau(q)$ characterizes the spatial "intermittency" or "irregularities" of the field [25]. On a soil moisture map, a lower "intermittency" field (lower τ) presents a more recognizable large-scale pattern with less local concentration. On the other hand, a higher intermittency field, typically associated with drier days, is more random, patchier, with less apparent structure and higher values (closer to 2) of τ. We use $\tau_{z1:z2}(q)$ to denote the qth order scaling exponents calculated for the layer between depths z_1 and z_2 (cm). To improve clarity, we will focus on $\tau_{0:\ 10}(2)$.

For this paper, we run our numerical model ([Section 2.3](#)) at the finest support scale, λ_{min}. Moments at support scale λ are obtained by aggregating simulated data from λ_{min}.

2.2. Multi-fractal models

Mascaro et al. [25] employed a multi-fractal model (MFM) to describe the theoretical expectation for τ as a function of q, drawn from simulated rainfall fields [54]:

$$\tau(q) = c\frac{q(1-\beta)-(1-\beta^q)}{\ln 2} \tag{3}$$

where c and β are fitting parameters. When $\beta = 0$, Eq. (3) describes a monofractal, and a multifractal otherwise. Mascaro et al. [20] further related c to field mean moisture:

$$c = c_\infty + \delta e^{-\lambda \bar{\theta}} \tag{4}$$

Alternatively, we also attempted the linear model:

$$c = b + a\bar{\theta} \tag{5}$$

where c_∞, δ, λ, a, and b are fitting parameters they attributed to environmental factors such as soils and slopes. Eqs. (3) and (4) predict that τ will be higher when the field is drier, consistent with our understanding that drier days are associated with higher intermittency. For each simulated moisture field, a set of c and β can be obtained by fitting Eq. (3) to extracted $\tau(q)$. Following Mascaro et al. [20], we fixed β while calibrating c. Then, we examined the relationships between c and $\bar{\theta}$ to evaluate whether Eqs. (4) and (5) are appropriate.

2.3. PAWS+CLM

PAWS (Process-based Adaptive Watershed Simulator) [47], [55], [56] is a computationally-efficient, physically-based hydrologic model that has been coupled with the community land model, CLM4.0 (hereafter called PAWS+CLM; Fig. 1). PAWS+CLM explicitly solves physically-based governing equations for 2D overland flow, 1D flow in channel network, quasi-3D subsurface flow, wetlands, and the dynamic, two-way interactions among these components. The quasi-3D subsurface flow is an approximation to the 3D Richards equation, with vertical soil water flow governed by a series of 1D Richards equation, which are coupled to the saturated quasi-3D groundwater flow at the bottom using a physically consistent boundary condition [55]. By reducing the dimensionality of the fully three-dimensional (3D) subsurface problem, the model significantly reduces computational demand with little loss of physics representation. PAWS+CLM emphasizes subgrid mechanisms (e.g., lowland depressions, overland-channel exchange) that attempt to account for lack of spatial resolution.
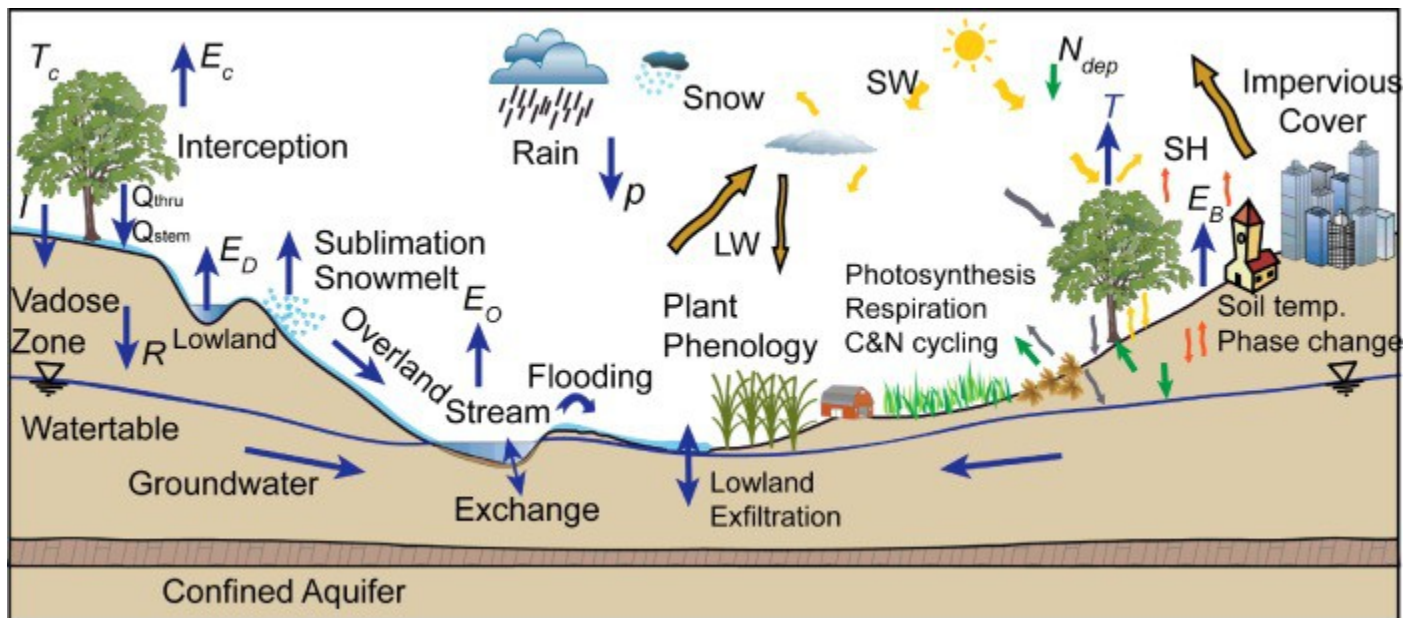
Download high-res image (609KB)
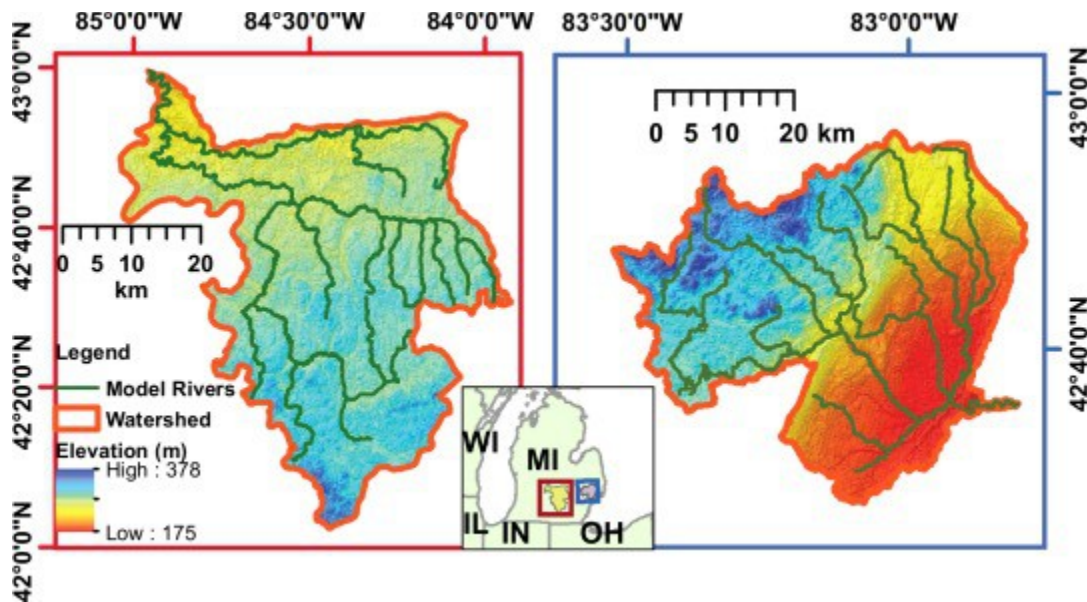Download full-size image

Fig. 1. Definition sketch of PAWS+CLM. This figure is modified from Fig. 1 in [55] and the CLM processes have been added. Blue arrows indicate water fluxes; yellow arrows indicate short-wave radiation fluxes; brown arrows with outlines indicate longwave radiation; orange arrows indicate heat fluxes; gray arrows indicate carbon fluxes and green arrows are nitrogen fluxes. Abbreviations: E_D: evaporation from depression storage; E_o: evaporation from channels; E_c: canopy evaporation; I: infiltration; R: recharge; P: precipitation; T: transpiration; T_c: canopy temperature; E_B: evaporation from bare ground; Q_{thru}: through flow; Q_{stem}: stemflow; N_{dep}: nitrogen deposition; SW: short-wave radiation; LW: long-wave radiation; SH: sensible heat. Carbon and nitrogen fluxes were not annotated to avoid clutter. Un-annotated terms include carbon storage and allocation, litterfall, soil respiration, mineral nitrogen uptake, denitrification, and leaching. (For interpretation of the references to color in this figure legend, the reader is referred to the web version of this article.)

CLM [57], [58] is a comprehensive land surface model encompassing energy and radiation cycles, hydrology, momentum/vapor/heat transfers, soil temperature, freeze and thaw, prognostic vegetation phenology, carbon and nitrogen cycles, and many other processes, through mostly mechanistic descriptions. The energy, momentum, vapor transfers and photosynthesis are solved simultaneously. The soil water flow and groundwater components in CLM have been replaced by PAWS components in the coupled model, while Evapotranspiration (ET) and soil freeze-thaw is calculated by CLM modules and passed to PAWS. Because PAWS is coupled to CLM4.0 (and soon to CLM4.5 [59], [60]), we can explicitly investigate interactions between carbon and nitrogen biogeochemical and hydrological dynamics.

PAWS+CLM has shown consistently good performance when compared with many observations from seven basins. The model obtained good Nash-sutcliffe performance coefficient on streamflow (Nash) in U.S. Midwest basins (1140 km^2 to 22,260 km^2), from 0.6 to 0.75 for calibrated and uncalibrated gages. In the 1837 km^2 Clinton River basin [47], we obtained a Nash of 0.61 at the calibration gage and 0.65 at an internal gage, partially influenced by increased missing climatic records after 2006 and the climate station unable to capture a large storm in 2004. Moreover, the R^2 between observed and simulated depths to water table (*wtd*) and soil temperature was 0.66 and 0.97, respectively. The baseflow was shown in log-scale plots to be better captured than peak flows, yielding higher Nash based on root-square-transformed data. In addition, the soil moisture [9], Leaf Area Index (LAI), and ET were shown to be in general agreement with *in-situ* and satellite-based observations. Similar good performance with different variables was achieved also in the 14,431 km^2 Grand River basin and the 22,556 km^2 Saginaw River basin [61]. In that study, the model agreed well with terrestrial water storage anomalies from GRACE data [62], and time series of groundwater table ($R^2 = 0.72$), streamflow, ET and soil moisture.

2.4. Study sites and model setup

In this paper we applied the PAWS+CLM model to two U.S. Michigan basins (Fig. 2a and b): the Clinton River Basin (CRB, 1837 km^2) and the Upper Grand River Basin (UG, 4531 km^2). The two basins share similar humid continental climate, with strong seasonality and an annual average precipitation input of ~900 mm $year^{-1}$, but they have different topography. The UG has very mild terrain (elevation: 195–355 m) and unconsolidated glacial drift surficial geology (moraines and tills) underlain by transmissive Marshall and Saginaw formations (fractured sandstones and shale), while the CRB (175–366 m) has rugged hills in the western half of the basin descending to a flat plain in the eastern half. The CRB also has glacial drift surficial geology, but it is underlain by low-permeability coldwater shale formations. Both CRB and UG have "patchy" soil spatial aggregation pattern (Fig. A.1 shows the distribution of clay percentages in the CRB), as in many other basins. There are higher percentages of fine-texture lacustrine sediment in the southeast, near the Lake St. Clair, due to lake deposition. As discussed later, we found the soil texture spatial aggregation pattern to be important for the fractal evolution during rainfall hiatus.

Fig. 2. Map of the two basins studied: (a) Upper Grand River Basin (UG) and (b) Clinton River Basin (CRB) in Michigan, USA. The CRB has rugged hills in the western half and a lowland plain in the eastern half, and is adjacent to the Lake St. Clair to the east. The UG has mild relief and lacked the topographical contrast in CRB.

Throughout the paper, we present results from the CRB, and include discussion about the UG in Section A.2. To focus our analysis on the temporal dynamics and basins' SMSF responses, we followed the approach of Gaur and Montanty [63] by using homogenized climatic input from one representative station in each basin (Oxford MI, COOPID 206303 for CRB and East Lansing, COOPID 202395 for UG). We acknowledge that spatial patterns in precipitation may have important influence at larger scales on soil moisture distributions [12] and modality [64].

We applied PAWS+CLM at 220 m × 220 m horizontal resolution (λ_{min}) for the CRB and 400 m × 400 m resolution for the UG, leading to 256 × 280 and 270 × 240 grids, respectively. We used 20 vertical soil layers with variable thicknesses: layers are thinner near the surface and thicker near the bedrock. Both basins were parameterized using similar input sources. The 30-m resolution National Elevation Dataset (NED) was used to generate cell elevation, river bed elevation, and lowland storage bottom elevation in each gridcell. The 30-m resolution IFMAP 2001 land use and land cover data [65] were aggregated to provide Plant Functional Type (PFT) information, with three dominant land use types (PFTs) in each cell. The 1:24,000 SSURGO dataset [66] was processed by a hierarchical pedotransfer function (PTF), Rosetta [67], to provide water retention and unsaturated vertical conductivity parameters for the vadose zone. We obtained the spatial maps of lateral conductivities of the unconfined aquifer (glacial drift) and depths to bedrock by interpolating well records from the WELLOGIC database [68], [69], [70] using Kriging.

Table 1. Codes of simulations.

Abbreviations	Procedures	Objectives
ctrl	Use the baseline parameters; weather input in the basin was set as from one single station	To show seasonal and rainfall-induced dynamics with less noise

Abbreviations	Procedures	Objectives
rs	The soil textures were reshuffled and randomly placed in the domain, breaking existing spatial autocorrelation	To demonstrate the effects of soil texture pattern on scaling exponents
hl	LULC was uniformly set to Deciduous Broadleaf Forest (DBF)	To show the effects of LULC spatial pattern on scaling exponents
hd	Initial water table was homogenized to the average water table depths in the basin	To reduce the impact of initial conditions on -GW and -nGW comparisons
storm	Based on *ctrl*, some precipitation events were removed	To present two prototypical rainfall-induced cycles
noForcing	Based on *ctrl*, source terms (ET and precipitation) were removed.	To show effect of basin self-organization
res2	Based on *ctrl*, grid resolution reduced in half	To show the effect of grid resolution on analyzed scaling exponents
nGW	Lateral groundwater flow was disabled by setting aquifer conductivity, K, to $1e{-}14$ m day^{-1}	To show the effect of having no lateral groundwater flow
GW	Groundwater flow was enabled and K was given the original input values	

The model was calibrated using root-transformed Nash–Sutcliffe model performance coefficient by adjusting global multipliers. The procedures and comparisons are given in Shen et al. [47]. A warm-up period was provided from 2001 to 2004, and we only examine the results after 2004.

2.5. Numerical experiments and analysis

We designed a series of numerical experiments highlighting the effects of soil texture and regional groundwater flow on the evolution of the fractal exponents (Table 1). In our previous study in the region, we identified soil texture, groundwater flow, and land use/landcover (LULC) as controls of soil moisture [71]. Therefore, we adopted a factorial experimental design, in which these three factors were enabled or disabled to examine their effects on the SMSF. For LULC, we considered both the original input data and a homogenized landscape (*hl*) with only deciduous broadleaf forest. For soil texture, we considered both the original input and a reshuffled soil texture (*rs*), in which the positions of the original soil textures were randomly switched in the watershed to eliminate any spatial autocorrelation and correlation with topography and LULC. For each combination of LULC and soil texture inputs, we conducted experiments with (a) groundwater flow enabled (*GW*); and (b) lateral groundwater flow disabled (*nGW*) by setting lateral groundwater conductivity, K, to 0. As we modify the K values, the steady state water table position also changes, and it will take many

simulation years for the model to re-establish near-equilibrium water table. To reduce the effects of initial data, we considered simulations with the initial water table depths of all simulations set uniformly to the basin-average values (*hd*).

We developed software utilities to export simulated daily-averaged soil moisture fields and calculate $\tau(q)$ from the fields. Simultaneously calculated were the moments of the fields. For the CRB, we divide the basin into roughly two halves: the western hills and eastern plain. We also distinguish between frozen and non-frozen periods, since the SMSF behaved dramatically different between the two periods ([Section 3.1](#)). We define the non-frozen period as the first day with soil ice after April 1st to the last non-frozen day before October 31st. For all the simulations listed in [Table 1](#), we computed scaling exponents and calculated the temporal average and standard deviation for non-frozen period for the entire basin. For the CRB, we also calculate the temporal mean and standard deviation of $\tau(q)$ for the two sub-domains.

Several numerical simulations were also designed to demonstrate the temporal evolution of the scaling exponents under idealized situations. Simulation *noForcing* shows how τ evolves in the absence of ET and rainfall, thereby allowing the basin to purely re-organize via vertical soil moisture movement and groundwater flow. Baseflow and exchange with lowland depressions were still allowed to occur. Such a scenario would obviously never happen, but it helps illustrate the isolated effects of groundwater flow on $\tau_{0:\,10}(2)$. In *noForcing*, following a precipitation event on July 15, 2006, ET or precipitation inputs were stopped from July 16 onwards. To show the typical temporal evolution trajectories of scaling exponents during and after storm events, we ran a hypothetical simulation, storm, which is identical to the control simulation (*ctrl*) except that precipitation inputs are modified to allow the excursions to evolve without disturbance from new storm events. The precipitation amounts on two starting days have been set to 32 mm and the storms following these two events were removed to produce two complete, un-interrupted cycles.

In addition, we also conducted experiments to examine the impact of grid resolution on our results. The CRB simulations were conducted using 220 m spatial resolution simulation (resulting in 256 × 280 × 20 grid cells). It was currently computationally difficult to run at higher resolutions. Therefore we ran simulation *res2*, which used a coarser grid (λ_{min} = 440 m).

3. Results and discussion

First, we verified the scale-invariance of the simulated soil moisture spatial field by examining the relationships between the spatial moments and the observation window size ([Section A.1](#)). We noted that there were a range of scales where the log–log linear relationship held true, and the upper-limit of the scale-invariant relationship (λ_{max}, fractal cut-off) was related to the size of the computational domain, so we always calculated the log–log slopes using data below λ_{max}. In the following, we first examine the fractal temporal evolution on a seasonal time scale. Then we demonstrate the influence of groundwater flow on the scaling exponent. Then we focus on how the fractal evolves during rainfall and rainfall hiatus. Subsequently, we show how the scaling exponent is related to variance, how grid resolution influences the results, and confirmation results from the UG.

3.1. Seasonal dynamics of the SMSF scaling exponent

Time series of the scaling exponents of top 10 cm soil moisture in the CRB basin have very different dynamics between summer and winter ([Fig. 3](#)a); similar differences occur in the UG basin ([Section A.2](#)). We identified common seasonal and event-driven patterns in the time series for both basins: (a) a slowly varying seasonal mode during the non-frozen period, in which $\tau_{0:10}^{2}$ increased from spring to summer, and declined back down during the cooler season when the basin is wetting; (b) short-lived spikes to near maximum values during the winter due to freezing; (c) storm-induced disturbances

superimposed on the non-frozen seasonal trend, creating first a small peak, which in a few days reverted to a dip, and then merged into the seasonal mode (Fig. 3a subpanel).
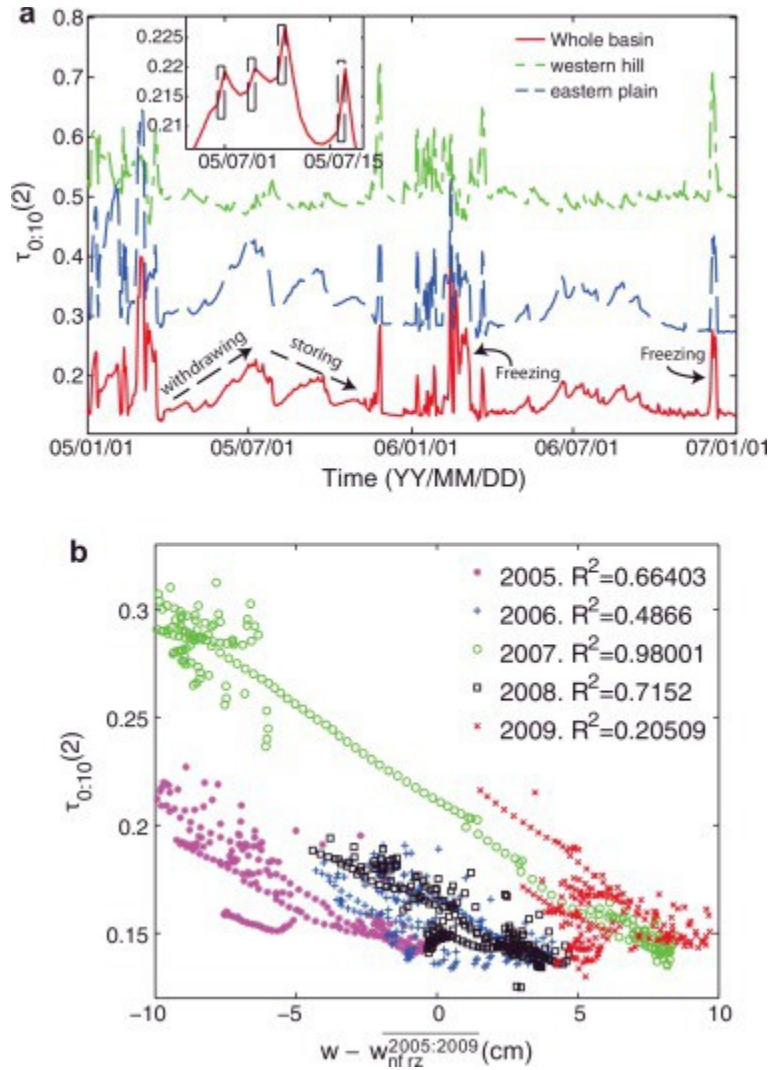
Fig. 3. (a) Time evolution of the scaling exponents in the CRB. The seasonal withdrawing and storing limbs and the effects of freezing have been annotated. The subpanel zooms into June, 2005 on the whole basin time series. The dashed boxes indicate days with rainfall; (b) Relationship between $\tau_{0:10}(2)$ and basin-average water storage (w) anomaly during non-frozen period (April–October, nfrz) in 2005–2009.

Since $\tau_{0:10}(2)$ is related inversely to the spatial organization of the moisture field, pattern (a) suggests that the field was most organized (or, "connected") during wetter seasons and that the structure gradually weakened during the summer dry-down, which is consistent with the observations from aircraft-based remotely-sensed data [20]. The non-frozen period fractal exponent is related to seasonally-varying basin states, and in particular basin water storage. This pattern is consistent with the model Mascaro et al. [20] applied, where mean soil moisture was used a predictor. There was a strong negative correlation between $\tau_{0:10}(2)$ and non-frozen period basin-average subsurface water storage (w, in cm) anomaly (defined as water storage minus 5-year mean; Fig. 2b) in each year except for 2009, with R^2 ranging between 0.48 and 0.98. R^2 in 2009 was only 0.21, perhaps because this was a particularly wet year, and therefore the effects of dry-down periods were weak. Water storage in this region generally declines during Spring and Summer and increases during Fall and Winter [47]. As a result, there are two seasonal limbs to the fractal $\tau_{0:10}(2)$ dynamics: the

"withdrawing limb" and the "storing limb" (marked in Fig. 3a). In the withdrawing limb (early Spring to Summer), water is being withdrawn from the basin, and $\tau_{0:10}(2)$ increases. In the storing limb (end of Summer through Winter), water is being stored in the subsurface and the scaling exponents decrease, with large variations occurring during freezing periods.

The scaling exponent for the entire CRB was consistently less than those for the two sub-domains. This pattern occurred because the entire basin showed more spatial organization than each sub-domain, due to the large contrast in soil moisture between the two sub-domains. Between the two sub-domains, the non-frozen period scaling exponent for the western hills was relatively more static in time and was generally higher than in the plain domain. The eastern plain sub-domain has in general higher soil moisture than the western hills due to basin-scale groundwater flow providing subsidy from the west to the east (Fig. A.2a and b; also [47]). There is a local spatial pattern within the plain sub-domain: the lower elevation region in the southeast has higher moisture than the northeast. In contrast, the moisture structure in the hills sub-domain is patchier and more isolated, mainly attributable to hillslope-valley contrasts, resulting in higher scaling exponents compared to the plains. The eastern plain domain also showed larger seasonal variation in $\tau_{0:10}(2)$ due to the shallower groundwater table, which was more strongly influenced by seasonal climate forcings. In a similar finding from field studies, Rosenbaum et al. [72] showed that groundwater-influenced areas (shallow water table) experience a larger range of spatial variance of soil moisture. In a percolation theory framework, Domenico and Laguardia [29] showed that, using another hydrologic model, the percolation probability is influenced by terrain morphology such as bifurcation and elongation ratios.

3.2. The impact of groundwater flow on scaling exponents

3.2.1. Impact on temporal mean and variability of τ

We now examine how the temporally aggregated τ behavior is influenced by groundwater, LULC, and soil properties. To reduce influence from initial conditions and present a fair comparison between with and without groundwater flow, here we plotted results from the simulations that homogenized the initial depth to water table (*-hd*). Fig. 4a shows that the temporal mean of non-frozen-period $\tau_{0:10}(2)$ declined dramatically with increasing physical controls (from right to left). Recall that a $\tau(2)$ value of 2 corresponds to a completely uncorrelated soil moisture distribution (i.e., white noise). For the case with reshuffled soil, homogenized landuse, and disabled groundwater flow, $\tau_{0:10}(2) = 1.97$, therefore representing a nearly random field with no spatial structure. Proceeding in the order of control (*cntl*), *rs-hd*, and *rs-hl-hd* (from left to right in Fig. 4a), more physical controls were added, and we observed a decreasing trend in $\tau_{0:10}(2)$. This pattern indicates that spatial structures form in the moisture fields as LULC heterogeneity and spatial soil texture patterns are introduced.
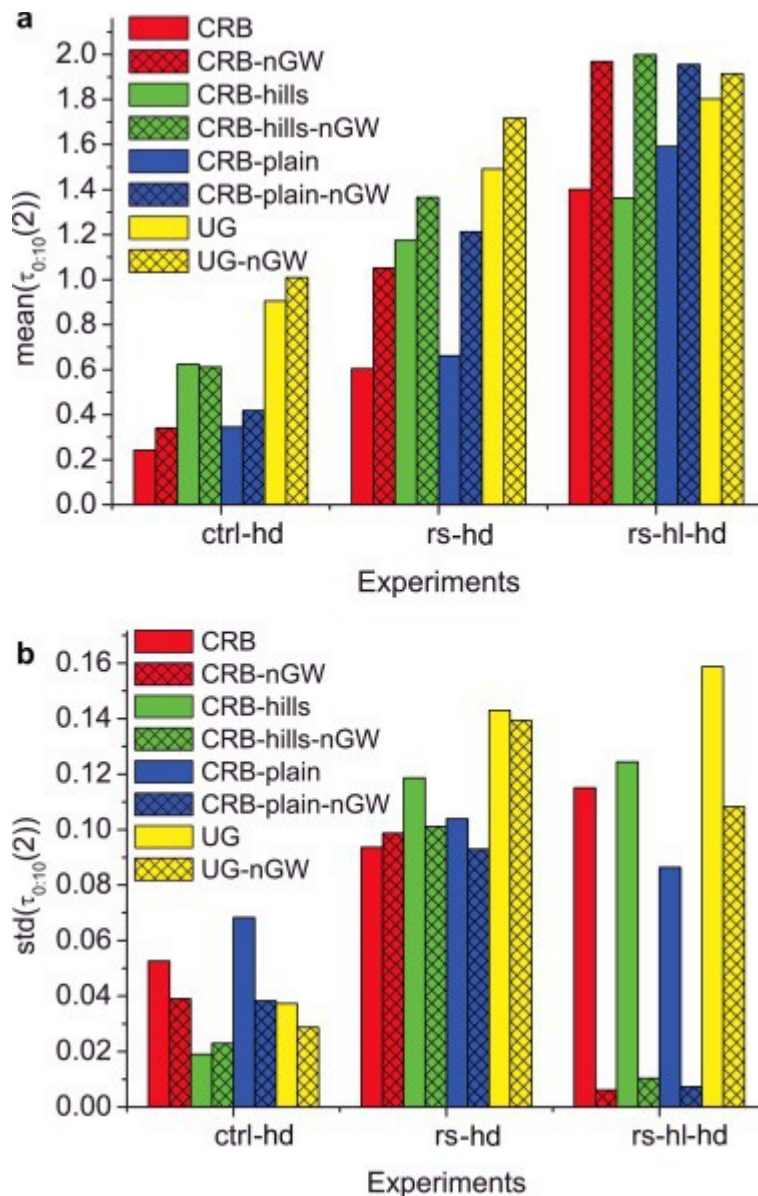
Fig. 4. (a) Temporal mean and (b) temporal standard deviation of $\tau_{0:10}(2)$ as a function of controls. The colors indicate domains. The solid-filled bars are groundwater enabled simulations (*GW*) while the hatched bars are groundwater disabled (*nGW*) simulations.

For all cases except for the hills sub-domain of the CRB, groundwater flow led to lower scaling exponents. However, the changes caused by groundwater flow were situation-dependent, and not predictable as an additive effect. Based on the control cases, where soil texture patterns were in effect, there was only a difference of ~0.1 between enabled and disabled groundwater flow. However, based on randomly-distributed-soil cases (*rs-*), which in general have much higher $\tau_{0:10}(2)$, there were differences in $\tau_{0:10}(2)$ of 0.19, 0.6, 0.4, and 0.22, respectively, for CRB-hill, CRB-plain, CRB-whole, and UG. This phenomenon may be attributed to how other controlling factors spatially co-vary with groundwater convergence patterns, yielding both correlated and anti-correlated interactions on moisture. Groundwater flow tends to induce higher moisture in lowland areas, foothills, and riparian zones, while wetter areas are often found with finer textures (clay) because they are better at retaining moisture. The two factors are sometimes correlated, as there are more clayey soils in the eastern lowland plains, especially near Lake St. Clair (Fig. A.1). Therefore the soil-texture-dominated pattern is correlated with the groundwater-dominated pattern. However, there can also be conflicting trends.

For example, near the stream riparian zones, where groundwater discharges, there is notably less clay. As a result, adding the groundwater flow in the *ctrl* cases yielded a smaller difference in τ, while adding it to the *rs* case yielded a much larger difference.

In addition to reducing the mean of $\tau_{0:\ 10}(2)$, groundwater flow also increased the temporal standard deviation of $\tau_{0:\ 10}(2)$, while the magnitude of the difference is also case-dependent (Fig. 4b). Higher standard deviation indicates stronger temporal variation of soil moisture pattern in response to climate forcings. Especially, for *rs-hl-hd*, when the dominant controls of soil texture and LULC were removed, groundwater alone contributed to the temporal dynamics of $\tau_{0:\ 10}(2)$. The corresponding temporal standard deviation of $\tau_{0:\ 10}(2)$ in the *rs-hl-hd-nGW* cases were all very small, suggesting that the pattern created by groundwater flow is very steady in time, while the soil texture-dominated pattern is very patchy.

3.2.2. Impact on the predictive formula

Since the Mascaro-2010 formulation (Eq. (3)) does not include groundwater, its effects can be implicitly accounted for during site-specific calibration using the $c \sim \theta^-$ relationship. Therefore, if groundwater flow substantially alters the $c \sim \theta^-$ relationship, we hypothesize that it can affect the transferability of the calibrated parameters. The $c \sim \theta^-$ (c as in Eq. (3)) relationships, based on daily data from several simulations, again highlight the complex interaction between the groundwater flow effects and other controls (Fig. 5). In Fig. 5a, the *ctrl-hd-nGW* points show a simple, generally decreasing relationship between c and θ^-, which can be well described by the linear function in Eq. (5). However, enabling groundwater flow (*ctrl-hd-GW*) introduced many hysteretic excursions which reduced the overall slope of the scattered points. The disturbance effect resulted from groundwater flow patterns not entirely matching the soil texture pattern, as explained in previous section. When soils were reshuffled, however, the $c \sim \theta^-$ completely changed, showing a positive correlation between c and θ^- in both *rs-hd-nGW* and *rs-hd-GW* simulations (Fig. 5b). Compared to *rs-hd-nGW*, *rs-hd-GW* has increased scattering of $c \sim \theta^-$ points in the lower c range. Further, when the LULC was uniformly set to a deciduous broadleaf forest, the contrast between *GW* and *nGW* simulations was more prominent (Fig. 5c): c and θ^- were positively correlated in *rs-hl-hd-GW* and negatively correlated in *rs-hl-hd-nGW*.
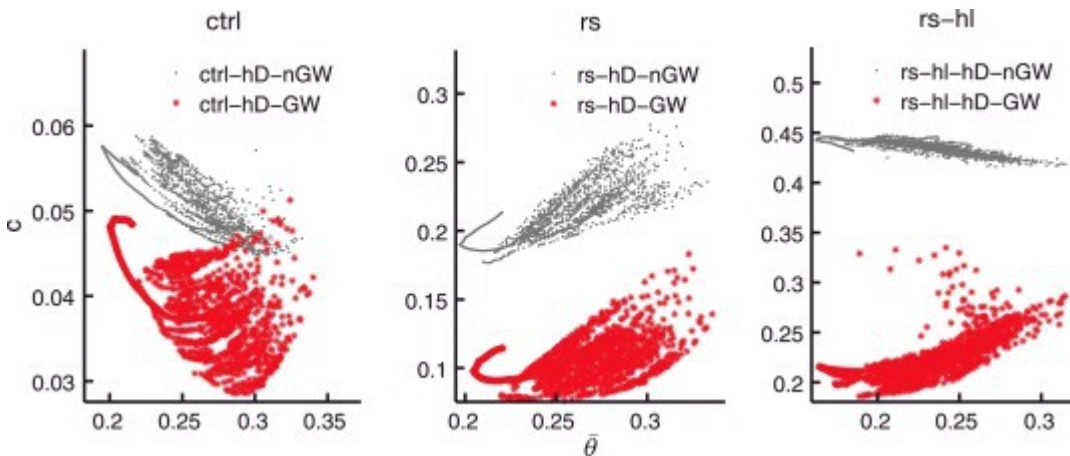
Fig. 5. Relationships between c and θ^- in the hypothetical simulations.

The complete change of behavior from Fig. 5a to b suggests that soil texture spatial distribution may be the primary factor responsible for the observed negative $c \sim \theta^-$ correlation found in the literature. Consider the rainfall hiatus, when θ^- decreases (going from the right of panel to the left in any panel in Fig. 5). With the original soil texture distribution (*ctrl-*), the moisture pattern was heavily influenced by small, isolated soil texture patches, leading to higher c. On the other hand, in a soil-reshuffled domain, the remaining dominant control besides groundwater flow is the LULC.

The smooth, large-scale structure induced by either LULC (e.g., due to canopy shading effects, evapotranspiration) or groundwater flow (due to topography) emerged as drydown occurs, leading to a more organized pattern and thus lower c. Consistent with this theory, in Fig. 5c, the $c \sim \theta^-$ was almost flat, as no factors introduce patterns, but when groundwater flow was added (*rs-hl-hd-GW*), it dominated, leading to positively correlated $c \sim \theta^-$.

3.2.3. Impact on the temporal evolution pattern

In *noForcing*, the model predicted a slow decline in τ, accompanied by a slow loss of water due to baseflow (Fig. 6a). The correlation between mean moisture and τ is strong after Day 0. In the absence of mass exchange with the atmosphere, the basin moisture continuously converged to lowland areas (hereafter termed the re-organization phase), leading to a stronger pattern and thus lower τ. In Fig. 6b, the decline in τ was fastest immediately after D0, and became gradually slower as re-organization proceeded. An analogous experiment with the UG showed a similar pattern (data not shown). Therefore, we can expect the fractal scaling exponent to gradually decrease as the basin releases water during recession periods. However, when the forcing terms (ET and precipitation) are present, the change in τ depends on the competing effects of inputs and re-organization.
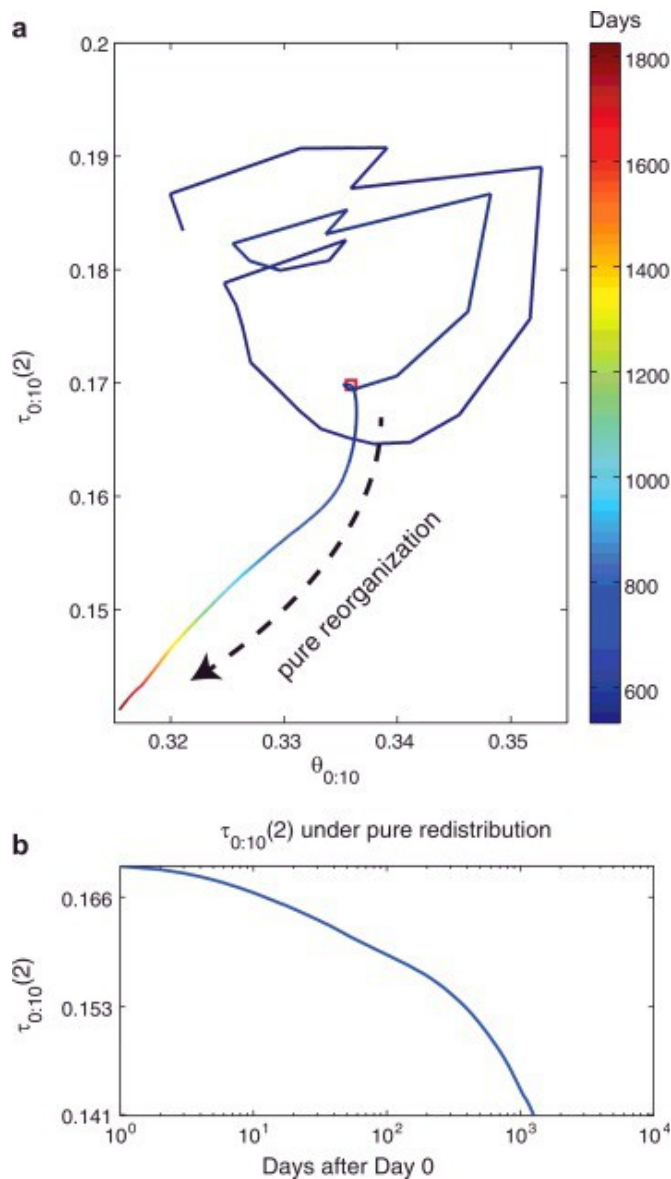
Download high-res image (279KB)
Download full-size image

Fig. 6. $\tau_{0:10}(2)$ evolution from *noForcing* where all water source terms (precipitation and ET) are set to zero on Day 0 (July 16th, 2006; Julian day 573 of the simulation; red square in (a)) and the basin is subject to pure redistribution. (a) $\tau_{(0:10)}(2)$ vs. $\theta_{0:10}$; (b) $\tau^2_{0:10}$ vs. time. (For interpretation of the references to color in this figure legend, the reader is referred to the web version of this article.)

In summary of the results in Section 3.2, soil texture seems to be a dominant controller of the $c \sim \theta^-$ relationship, and, as expected, the soil texture spatial distribution will be a primary contributor to the parameters describing this relationship. However, apart from soil texture and LULC, groundwater flow also introduces noticeable disturbances to the relationship, and characteristically alters the $c \sim \theta^-$ relationship. The calibrated parameters implicitly compensate for the groundwater flow, implying that its transferability may be limited. Therefore, the role of groundwater should be explicitly included in an improved predictive formula.

3.3. Rainfall-induced hysteresis

3.3.1. Typical τ response to rainfall and rainfall hiatus

In this section we examine how τ typically evolves during and after rain events. From Fig. 7a and b, note that the $\tau^2_{0:10}$ values were not a single-valued function of $\theta_{0:10}$. Rather, we observed loops and shifts of the $\tau^2_{0:10}$ orbits, indicative of system hysteresis. Hysteresis in the coefficient of variation vs. mean moisture state plane was also observed in simulations of an arid system [48], [73] and a humid temperature basin [72].

Download high-res image (578KB)
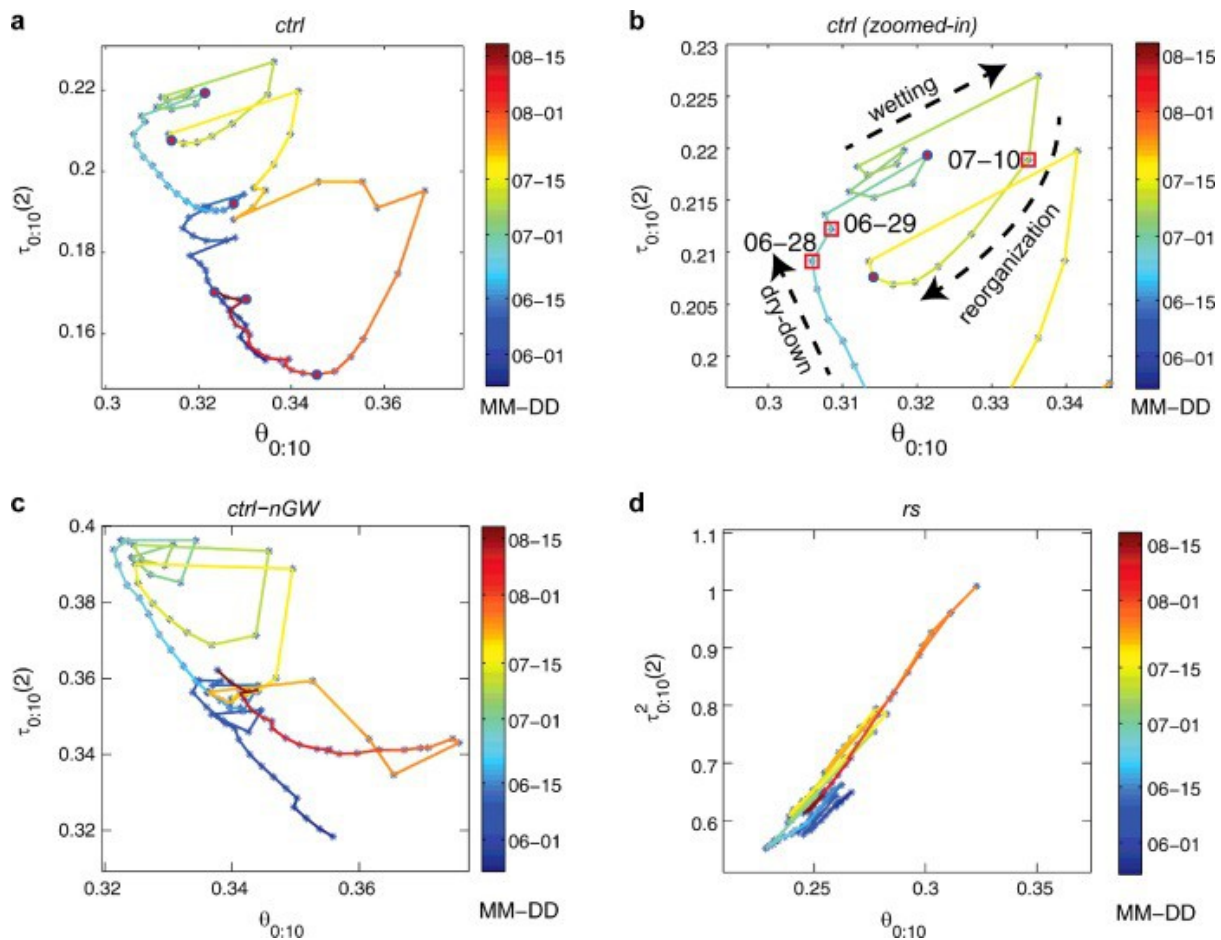
Fig. 7. (a) $\tau_{0:\,10}(2)$ vs. $\theta_{0:\,10}$ (top 10 cm layer soil moisture) orbits from May 24th to August 18th, 2005 for the *ctrl* simulation, with color indicating time; (b) Close-up of the upper half region of (a). The three phases of rainfall-induced excursion have been annotated. The red squares in (b) mark out points corresponding to three annotated days (MM-DD). Color of the lines in all panels indicates time (MM-DD); (c) and (d) same as in (a), but for, respectively, the groundwater disabled (*ctrl-nGW*) case and the reshuffled soil texture simulation (*rs*). When soil textures were reshuffled (LULC and groundwater flow are both in effect), $\tau_{0:\,10}(2)$ vs. $\theta_{0:\,10}$ relationship changed to positive correlation with little hysteresis, indicating that the patchiness of soil is the primary contributor to the hysteresis and inverse $\tau_{0:\,10}(2)$ vs. $\theta_{0:\,10}$ relationships observed in the field. (For interpretation of the references to color in this figure legend, the reader is referred to the web version of this article.)

These excursion loops can be broadly divided into three phases (Fig. 7b): (1) a wetting phase; (2) the subsequent 're-organizing'-dominated phase, shown as the curve bending downward in tau; and (3) a dry-down phase, where $\theta_{0:\,10}$ decrease steadily while $\tau_{0:\,10}(2)$ increases. After the re-organizing phase finishes, the hysteretic loop merges back onto the seasonal mode. As shown in Fig. 7b the curve slopes down along an almost constant slope on the $\tau_{0:10}(2)-\theta_{0}:_{10}$ plane during multiple reorganization periods. A storm event is easily spotted on Fig. 7a and b as a sudden excursion toward the right (increasing $\theta_{0:\,10}$), which then gradually bends its way back toward the left, along a separate path, until the next rainfall hits. Fig. A.2b shows the moisture field on June 28th, which was the last day of a dry-down phase. On the next day, June 29th, 2005, 3.56 mm of rain fell. The difference in 0–10 cm soil moisture between these two days ($\Delta\theta_{0:\,10}$; Fig. 8b) shows higher values in the highland hills in the West and North of the domain. Because these highland hills were much drier after a long drying phase, they were able to absorb more moisture as the storm hit than the lowland plains and local depressions. Therefore, rainfall acted to reduce the variability of the field, thereby very mildly weakening the $\theta_{0:\,10}$ spatial structure. Rainfall stopped on July 9th. Over the next three days, $\tau_{0:\,10}(2)$ declined and erased the "gain" during the rainfall (Fig. 7a). Basin redistribution immediately following rainfall strongly impacts these patterns (Fig. 8c). The redistribution is the emergent combination of infiltration, ET, and groundwater lateral flow. However, as we demonstrate in Section 3.3.2, the main factor contributing to the hysteresis is the spatial aggregation pattern of soil texture. Ensuing the redistribution, the dry-down phase started and the wet clusters became patchier (Fig. 8a shows the change in $\theta_{0:\,10}$ during a typical dry-down day), resulting in an increasing $\tau_{0:\,10}(2)$.
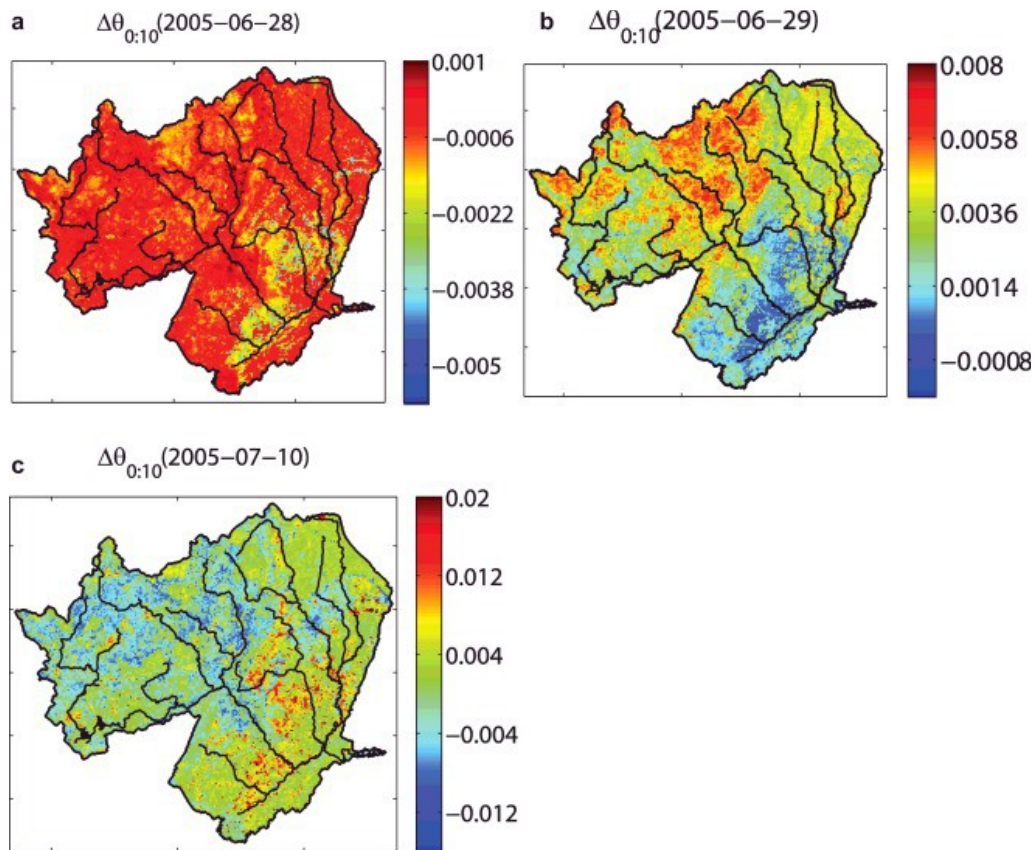
Fig. 8. Δθ=θ(t)−θ(t−1) on selected days in 2005 (these days are marked out by red squares on Fig. 7c) from *ctrl*: (a) 06-28: last day of a dry-down period; (b) 06-29: a small precipitation event (3.56 mm); (c) 07-10: first dry day after a large precipitation event.

3.3.2. Controls of hysteresis and temporal evolution

Orbits from hypothetical simulations clearly established that the soil texture pattern was the main cause of the rainfall-induced hysteresis (Fig. 7c and d). The simulations with reshuffled soil texture (*rs*) did not exhibit any hysteresis. Rather, the orbit showed a positive linear $\tau_{0:\,10}(2)$ vs. $\theta_{0:\,10}$ relationship, which is contrary to the *ctrl* case. The *ctrl-nGW*, on the other hand, has a strong hysteresis, and has maintained the negative $\tau_{0:\,10}(2)$ vs. $\theta_{0:\,10}$ relationship during dry-down. Therefore groundwater could not have been the main cause of hysteresis.

We attribute the hysteresis to different soils' infiltration and water retention behavior. Immediately after rainfall, moisture continues to infiltrate and re-organize as driven by pressure gradients. These processes tend to create smooth patterns that lead to lower τ. However, when the re-organization finishes, ET drives the dynamics as the rainfall hiatus continues. Finer texture soils are better at retaining moisture from evaporation and transpiration, and the patchy soil texture aggregation pattern emerges, therefore leading to higher τ. In the *rs*-simulations, as the patchy aggregation pattern does not exist, τ decreases during dry-down because of the organizing effects of groundwater flow and LULC.

The competing influence of multiple factors on τ can be qualitatively generalized into several phenomenological laws, as illustrated in Fig. 9. During rainfall hiatus, patchy soil texture spatial patterns produce hysteretic loops. Groundwater and LULC always tend to create regional structures and therefore lower τ. These phenomenological laws seem to work for all the cases we simulated for the two basins.
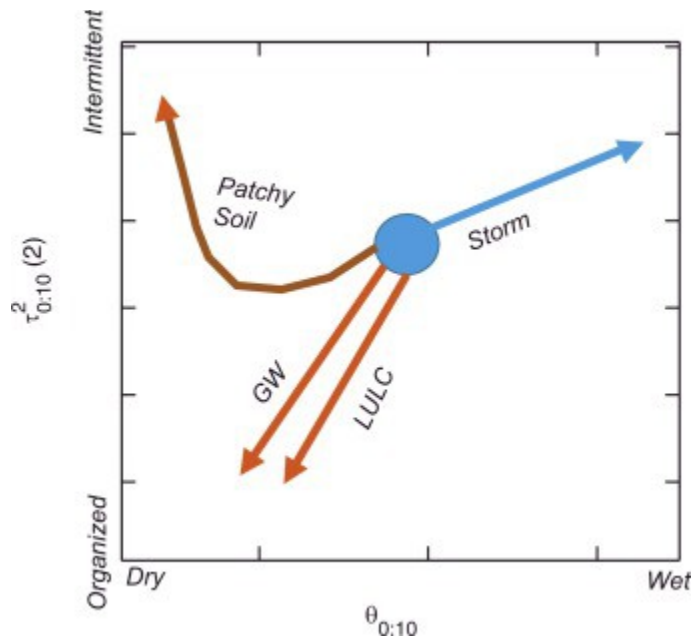
Fig. 9. Phenomenological behaviors of different competing processes acting on $\tau_{0:\,10}(2)$: the blue circle indicates initial state. The blue arrow shows the behavior of storm event. The brown arrows show the individual potential effect of groundwater flow (GW), land use land cover (LULC) and spatial aggregation of soil texture (Patchy soil) on fractal evolution during rainfall hiatus following the rainfall. When all factors are present, the system evolves according to the predominant factor (soils), but the effects of other factors are noticeable. (For interpretation of the references to color in this figure legend, the reader is referred to the web version of this article.)

In the *storm* experiments, for the withdrawing limb response (Fig. 10a), ET is strong, the re-organization phase is short-lived and under-developed, and the excursion quickly returns to the dry-down phase. For the storing limb response (Fig. 10b), the re-organization phase is longer, well-developed, the corresponding drop in τ is significant, and the effect of ET is small. It is through these long re-organization phases that τ returns to its annual lows. The shapes of the $\tau_{0:\,10}(2)$ vs. $\theta_{0:\,10}$ curves are qualitatively similar in the withdrawing and storing limbs, with the strengths of ET and precipitation determining the relative differences in the shapes.

Using 8 days of airborne ESTAR soil moisture data and simulation from a land surface model TOPLATS, which was coupled to TOPMODEL, Peters-Lidard et al. [74] also found similar three-phase responses which they termed "atmospheric/infiltration dominated", "transitional" and "drainage/evaporation dominated". During the last phase, they also found the scaling exponent increased. Due to the short length of the campaign, their data was limited. While their model did not explicitly simulate groundwater flow, our results are comparable and our phase-plane clearly illustrated the three phase response to storm as a general phenomenological rule. This fact provided further evidence that the hysteresis was due to soil properties. Moreover, we show that the rainfall response is embedded in the larger-amplitude seasonal cycle. Their study did not explain how physical processes (soil and landuse variability and groundwater flow) each control the evolution of the τ, their interacting effects, and their influence on the predictive formula. Nor did they examine the different behavior of the hysteresis loops in different limbs of the seasonal cycle. The results presented here should improve our understanding of the general rule of fractal evolution.
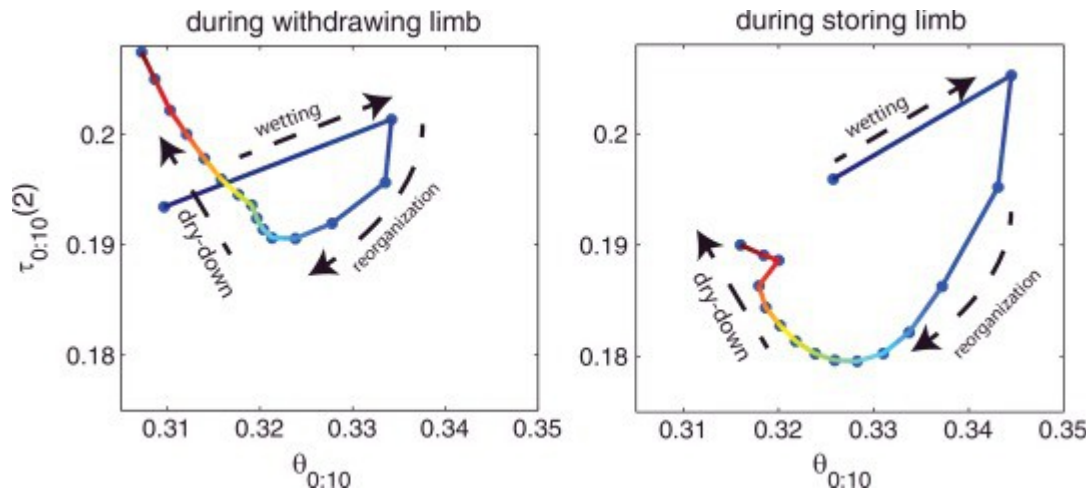
Fig. 10. Prototypical rainfall-induced excursions during (a) seasonal withdrawing limb and (b) seasonal storing limb. Colors indicate number of days after the last precipitation event and a dot indicates a single day. Both excursions include 17 dry days following the same precipitation amounts (32 mm) on day 1. For easy comparison, both panels are set to the same extent on $\theta_{0:10}$ and $\tau_{0:10}(2)$ axes.

3.4. Relationship between mean, variance, and the scaling exponent

Since an identifiable pattern must be supported by sufficient spatial variability, one may be tempted to think of τ as a proxy for variance. We show next that this is not the case ([Fig. 11](#)). Hysteretic loops between $\tau_{0:10}(2)$ and $\sigma^2_{0:10}$ are noted, suggesting complex and non-unique relationships between them. As compared to [Fig. 7](#), each storm event in [Fig. 11](#) is indicated by a straight movement toward the left with a slight increase in $\tau_{0:10}(2)$ but a significant drop in $\sigma^2_{0:10}$, in synchrony with increases in the mean moisture (color-coded), which agree with previous studies that showed variance decreasing due to storm events [48]. During the wetting phase, the $\tau_{0:10}(2)$ and $\sigma^2_{0:10}$ seemed to have a very stable linear relationship, as all wetting events show the same slope. During the re-organization-dominated phases, the orbit returned to the right along a different path than the wetting phases. The correlation between the two variables seemed to break down during the dry-down phases (notwithstanding a few smaller rainfall events), when the variance changed only slightly while $\tau_{0:10}(2)$ climbs substantially higher. This pattern suggests that $\tau_{0:10}(2)$ may be better at revealing internal structures of the field than variance. The change in variance seemed to 'stall' during the dry-down process, but the structural pattern continued to evolve. Although a direct mathematical explanation is not presently available, this result highlights the difference between variance and organization.
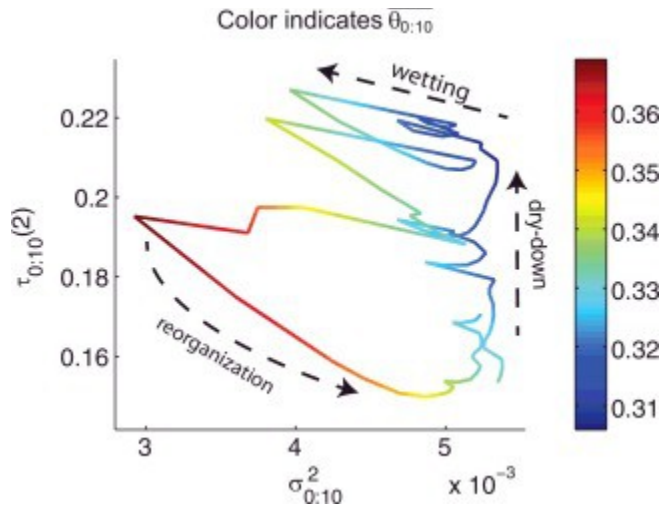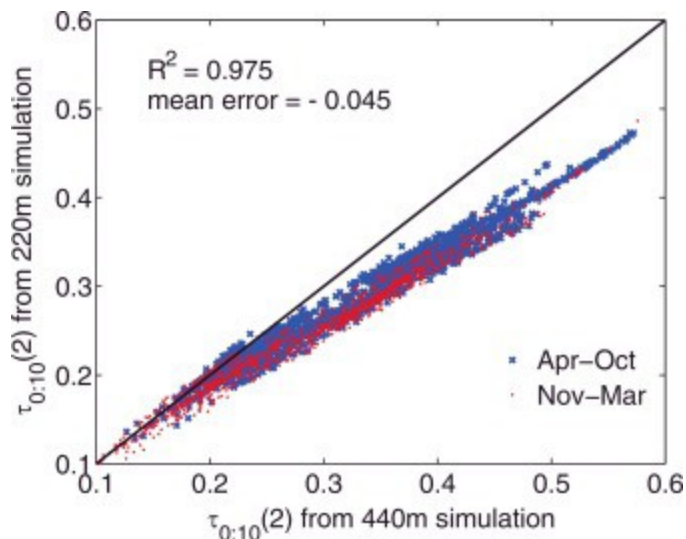
Color indicates $\overline{\theta}_{0:10}$

Fig. 11. $\tau^2_{0:10}$ vs. $\sigma^2_{0:10}$ with color of the line representing the mean moisture from May 24th to August 18th, 2005, the same days as in Fig. 7.

3.5. Effect of grid resolution (λ_{min})

In our resolution refinement analyses, the exponents from higher-resolution simulations (*res2*) closely followed the patterns from ctrl and the correlation was very strong ($R^2 = 0.975$) (Fig. 12). However, the fine resolution τ is always slightly lower than the coarser resolution one. We believe this pattern is due to the ability of the higher-resolution simulation to capture more fine-scale variability in elevation, which leads to more organization of the field (and thus lower τ). Nevertheless, the temporal pattern discussed in previous sections will still hold if we had used the 440 m simulation results. The strong correlation suggests it is possible to predict fine-resolution τ using coarser-resolution simulations, after applying some corrections to remove the negative bias, making a fractal-based multi-scale modeling approach more tractable.

Fig. 12. Effect of simulated grid resolution on $\tau_{0:10}(2)$ from 2002 to 2009. Two groups of points are shown: April to October each year, and November to March next year.

## 3.6. Implications for potential predictive formula for τ

Previous observational studies reported higher scaling exponent on drier days, and proposed that scaling exponents can be related to mean moisture and ancillary environmental predictors [25]. Indeed, this is a promising direction and our results also suggest that fractal exponents may be controlled by environmental factors. However, we note that caution must be exercised when prescribing a relationship between τ and mean moisture. As the hysteretic loops and seasonal limbs in Fig. 7 suggest, not only is there no simple 1-to-1 mapping between τ and θ, their relationship may also depend on seasonal basin water storage and phase position in the excursion. A static regression equation is therefore not likely to accurately capture these dynamics.
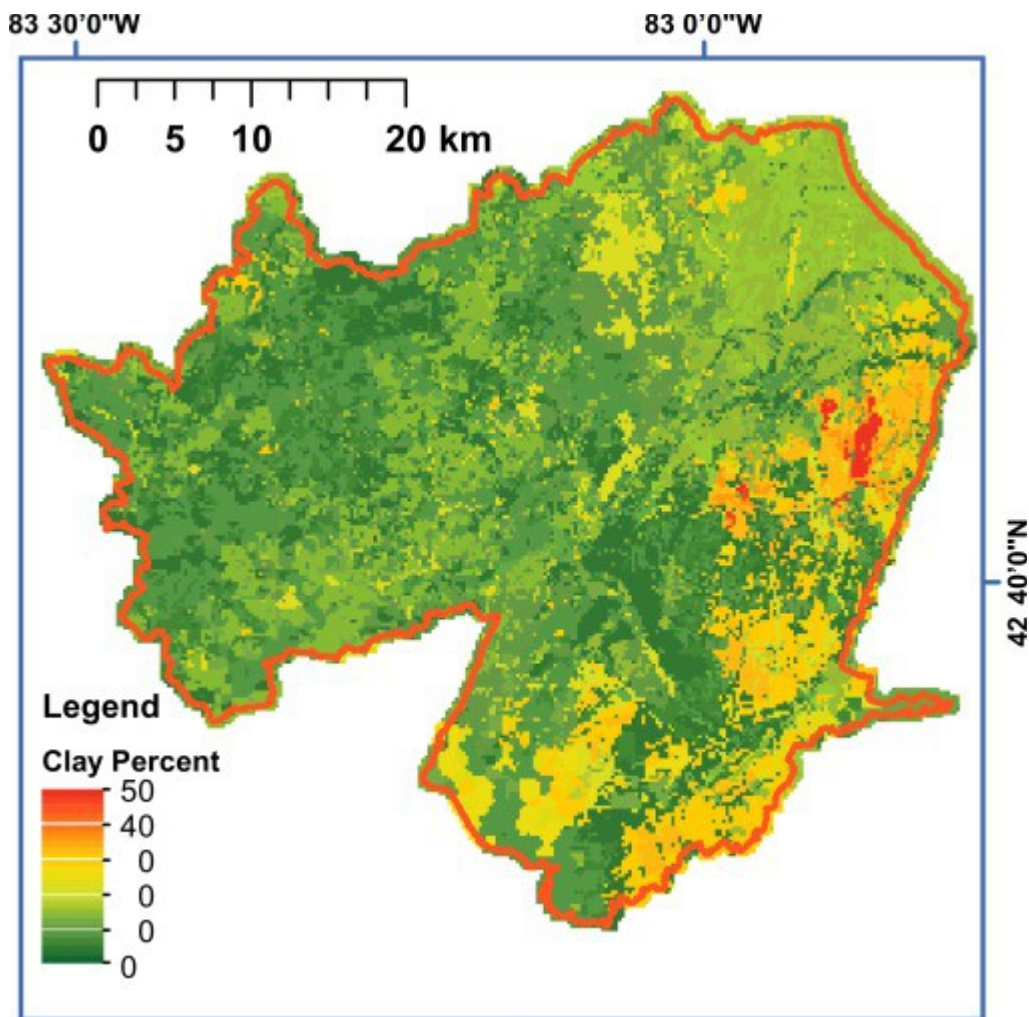
Fig. A.1. Map of top-layer clay percentages in the Clinton River basin.
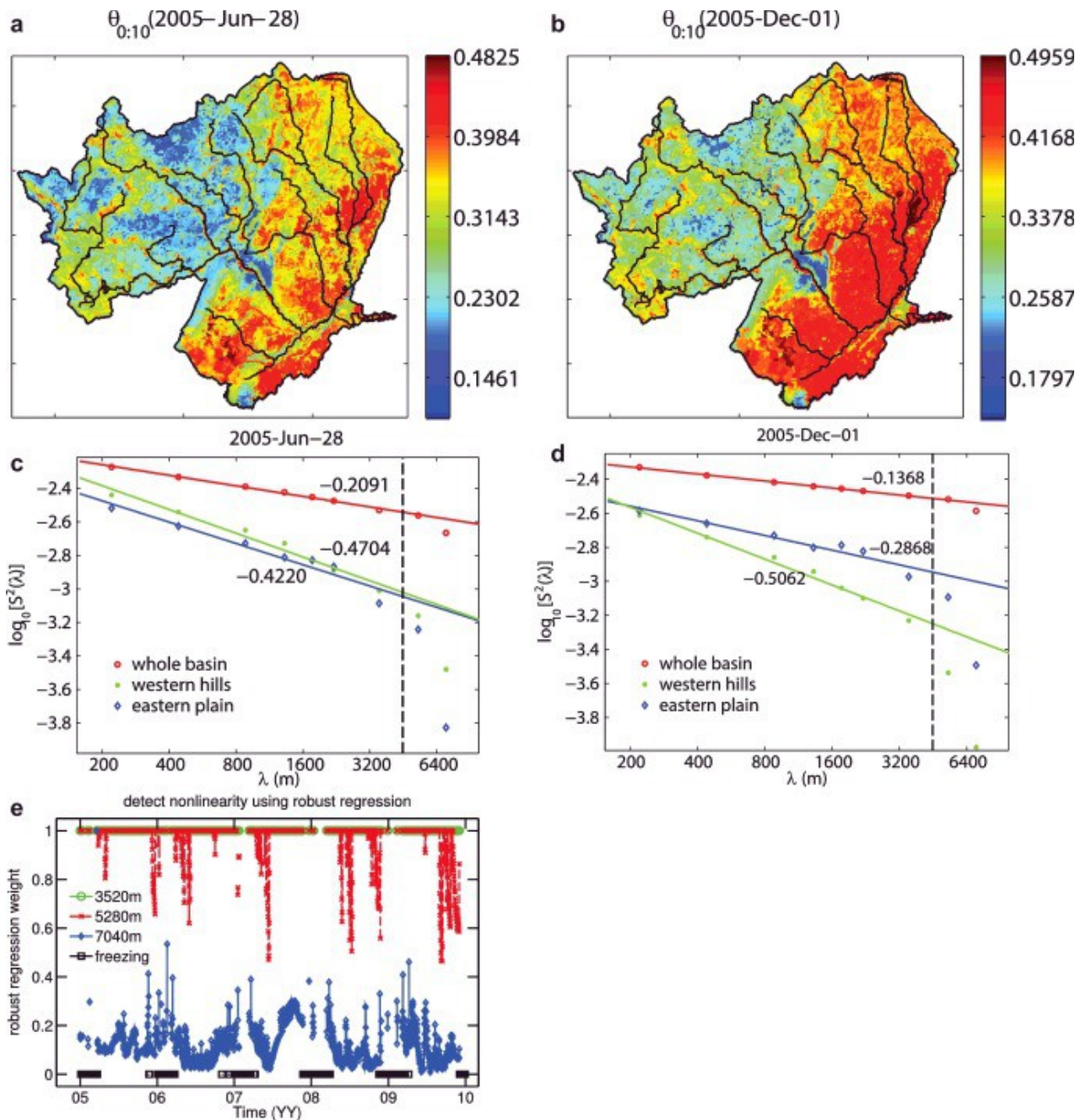
Fig. A.2. Spatial maps and related scaling of moments for the CRB: (a) θ0: 10 map on 2005-06-28; (b) $\theta_{0:10}$ map on 2005-12-01; (c) power-law decay of spatial moments in map (a); and (d) power-law decay of spatial moments in map (b). The black dashed lines indicate the fractal cutoff, above which the fractal relationship breaks down. Our estimation of scaling exponents uses only data below the cutoff threshold; (e) detecting nonlinearity using robust regression weights for the points corresponding to λ = 3520, 5280 and 7080 m window sizes, which shows that the 7080 m point is always above fractal cutoff, 5280 m point seasonally above cutoff, and 3520 m point always below the cutoff (never showed statistically significant nonlinearity). Therefore, we choose λ_{max} = 3520.

4. Limitations and future work

This study did not examine the relative impact of rainfall, humidity, wind speed, solar radiation, and temperature spatial variability on basin fractal evolution. It is known that rainfall fields also show multifractal scaling [54], making

interpretation of the impacts of watershed surface and subsurface properties on fractal scaling exponents substantially more complex. However, we argue that understanding the fractal exponent responses related to land properties is a first step toward understanding the overall system responses. Climate variability can play a significant role on the meso-scale (10 km), but there is still substantial sub-cell heterogeneity that can be addressed by fractal-based multi-scale approaches.

As in other modeling studies, the results of this study are influenced by the model employed. Although we have utilized a well-tested physically-based hydrologic land-surface model, PAWS+CLM, all models have simplifications that may impact their predictions. For example, PAWS+CLM makes a simplifying assumption, for computational reasons, that moisture does not flow laterally above the fluctuating water table. This simplification may introduce errors where a shallow perched water table is important. Our current model also does not simulate hydrophobicity or soil shrinkage and swelling, which could be important for soil water bypass flow, and influence upslope soil water recharge. We expect different hydrologic models will produce somewhat different responses in fractal evolution, but do not expect qualitative changes.

Admittedly, the patterns we discovered through numerical studies are far from being applicable in a predictive formula, but it is an important step toward characterizing soil moisture fractal evolution. Synthesis of observed patterns and behaviors (and, in our case, patterns from numerical simulations) is an important approach toward a coherent body of knowledge [75]. For example, given that the scaling exponents better reflect the moisture organization than variance (Section 3.4), future work may consider using this knowledge and the observed scaling exponents (e.g., from satellite observations) to infer the phase of soil moisture dynamics.

5. Conclusions

In general, groundwater flow introduces large-scale spatial patterns in near-surface soil moisture and therefore reduces the fractal scaling exponents and increases their temporal variation. However, the complexity lies with the interaction and covariation between groundwater and other physical controls, which may limit the transferability of calibrated parameters. These interactions make it difficult to propose a general predictor-based formula for the scaling exponents.

We identified a seasonal mode that is related to seasonal variation in basin water storage, while storm events induce hysteretic excursion loops which can be divided into wetting, re-organization-dominated, and dry-down-dominated phases. A predictive formula for the scaling exponents will likely need to include phase-dependent terms. The responses of τ to climatic forcing seem to generally follow a set of phenomenological rules. All of our simulations in the two basins agree with these rules, and their applicability can be examined in other basins. Although in this study we made no attempt to propose governing equations to describe these rules, they have the potential to help us develop such a predictive formula. The hysteresis is shown to be due to heterogeneous infiltration, basin self-organization of moisture, and, more importantly, soil texture spatial aggregation. The more "patchy" the soil texture, the higher the fractal scaling exponents will be. Topography and groundwater flow play important roles in modulating the fractal evolution.

Acknowledgments

Appendix A

A.1. Evidence of scale invariance in simulated soil moisture fields

The clay percentages in the CRB have been shown in Fig. A.1. As we can see, the spatial aggregation of soil texture tends to be patchy, showing many small clumps. This is an important factor determining fractal evolution. To illustrate the validity of the scale-invariance assumption, we show the spatial fields of soil moisture (liquid phase only) on two days of the simulation in the CRB and the related power-law decay of spatial moments in Fig. A.2, for both the whole basin and the sub-domains. Although both panels show a large-scale moisture gradient, the contrast is larger in Fig. A.2b (December 01, 2005). The eastern lowland on average was much wetter than the Western hills due to groundwater lateral redistribution. The soil moisture field on the lowland was also smoother. June 28, 2005 represents a day with large $\tau_{0:10}(2)$, when soil moisture was near the driest in the year. December 02, 2005 represents a day with low $\tau_{0:10}(2)$, showing a stronger large-scale contrast between the western half and eastern halves of the basin.

In the whole basin and the two sub-domains there are a range of scales where the log–log linear relationship holds true. We also notice an upper-limit of the scale-invariant relationship (λ_{max}, fractal cut-off), indicated by the dark dashed lines, beyond which the scaling curves deviate from a linear relationship. For the CRB (basin area of 1837 km^2), λ_{max} has been determined to be around 3520 m after examining the scale-invariance plot (Fig. A.2) from a random sample of 30 days of simulation. In addition, for the whole time series, we have verified there is no statistically significant departure from the linear trend within the fractal cut-off. On each day, a robust regression with the Huber weighting function [76] was applied to the data. The Robust regression iteratively reweights the data points to check for violation of assumptions of least squares fit, e.g., outliers, or nonlinearity, which will be assigned lower weights in the fitting. Thus, a low weight (here we take as <0.9) for a data point indicates that it fell off the scale-invariance relationship. From the time series of the weights (Fig. A.2e), the $\lambda = 7080$ m point was always considered an outlier (due to nonlinearity); the $\lambda = 5280$ m point was assigned low weight only during driest parts of the year, and the weight for point $\lambda = 3520$ was always above 0.98. Therefore, it was reasonable to set λ_{max} as 3520 m. Similarly, for the UG (4531 km^2, data not shown here), λ_{max} is around 9000 m. We believe this divergence from linear scaling is due to the limited size of our basins, and not an intrinsic property of the scaling structure. All scaling exponents are estimated from scales $\in [\lambda min, \lambda max]$.
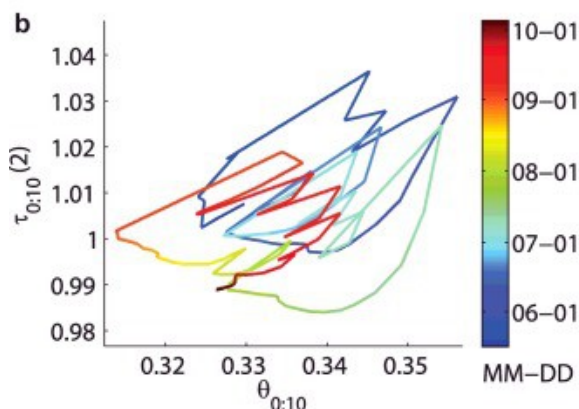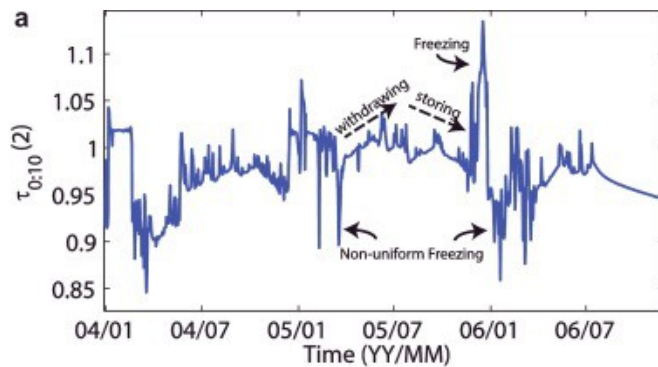
Fig. A.3. (a) Time series of $\tau_{0:10}(2)$ in the UG in 2004–2006 and (b) $\tau_{0:10}(2) \sim \theta_{0:10}$ between May 30th and October 18th, 2005. Similar to the CRB, we notice seasonal withdrawing and storing limbs, and rainfall-induced excursions, although the range of $\tau_{0:10}(2)$ is smaller with the UG.

A.2. Results from the upper grand

The UG basin has similar climatic forcing but different topography than the CRB. Fig. A.3a shows the time series of $\tau_{0:10}(2)$ from UG and Fig. A.3b shows the $\tau_{0:10}(2) \sim \theta_{0:10}$ plot in 2005, also from a weather-homogenized simulation. Generally, the results were similar to those from the CRB, with some differences. First, $\tau_{0:10}(2)$ was much larger than the CRB, but with a tighter range, varying between 0.95 and 1.05. We attribute the larger τ values and smaller variation to (a) much patchier soil texture, especially in the upper basin; and (b) lack of large-scale topography patterns in the UG, which does not have a hill-plain contrast as the CRB does. As a result, the large-scale pattern was weak and moisture patterns in the UG were more spatially intermittent and appear more like scattered islands [21] compared to the CRB. The model did predict seasonal withdrawing and storing limbs, and the significant impacts by freezing. The model also predicted rainfall-induced excursions. Fig. A.3b shows many rainfall-induced excursions between May 30th and October 18th, 2005, which are similar to those observed in the CRB. The rises accompanying the storm events were larger than those in the CRB, perhaps due to the milder terrain, which can lead to stronger 'homogenizing' effects by storms.

In the UG, freezing also caused more obvious downward spikes when only a clustered fraction of the domain froze, and created a temporary spatial pattern. For example, our model predicted that soil covered by forest froze earlier than urban and agricultural areas. When only the forested areas froze in the UG simulations, the soil moisture pattern created a downward spike in $\tau_{0:10}(2)$.

References

1. Paschalis A., Fatichi S., Molnar P., Rimkus S., Burlando P.
   On the effects of small scale space-time variability of rainfall on basin flood response
   J Hydrol, 514 (2014), pp. 313-327, 10.1016/j.jhydrol.2014.04.014
2. Heathman G.C., Cosh M.H., Merwade V., Han E.
   Multi-scale temporal stability analysis of surface and subsurface soil moisture within the Upper Cedar Creek Watershed, Indiana
   CATENA, 95 (2012), pp. 91-103, 10.1016/j.catena.2012.03.008
3. Brocca L., Tullo T., Melone F., Moramarco T., Morbidelli R.
   Catchment scale soil moisture spatial–temporal variability
   J Hydrol, 422-423 (2012), pp. 63-75, 10.1016/j.jhydrol.2011.12.039
4. Wilson D.J.Identifying and quantifying sources of variability in temporal and spatial soil moisture observations
   Water Resour Res, 40 (2004), pp. 1-11, 10.1029/2003WR002306
5. Entin J.K., Robock A., Vinnikov K.Y., Hollinger S.E., Liu S., Namkhai A.
   Temporal and spatial scales of observed soil moisture variations in extratropics
   J Geophys Res, 105 (2000), pp. 11865-11877, 10.1029/2000JD900051
6. Seneviratne S.I., Corti T., Davin E.L., Hirschi M., Jaeger E.B., Lehner I., et al.
   Investigating soil moisture–climate interactions in a changing climate: a review
   Earth Sci Rev, 99 (2010), pp. 125-161, 10.1016/j.earscirev.2010.02.004
7. Western A.W., Grayson R.B., Blöschl G.
   Scaling of soil moisture: a hydrologic perspective
   Annu Rev Earth Planet Sci, 30 (2002), pp. 149-180, 10.1146/annurev.earth.30.091201.140434
8. Famiglietti J.S., Ryu D., Berg A.A., Rodell M., Jackson T.J.
   Field observations of soil moisture variability across scales

Water Resour Res, 44 (2008), p. W01423, [10.1029/2006WR005804](10.1029/2006WR005804)

9. Riley W.J., Shen C.
Characterizing coarse-resolution watershed soil moisture heterogeneity using fine-scale simulations
Hydrol Earth Syst Sci, 18 (2014), pp. 2463-2483, 10.5194/hess-18-2463-2014

10. Pau G.S.H., Bisht G., Riley W.J.
A reduced-order modeling approach to represent subgrid-scale hydrological dynamics for land-surface simulations: application in a polygonal tundra landscape
Geosci Model Dev, 7 (2014), pp. 2091-2105, [10.5194/gmd-7-2091-2014](10.5194/gmd-7-2091-2014)

11. Wood E.F.
Scale analyses for land-surface hydrology
Sposito G. (Ed.), Scale dependence and scale invariance in hydrology, Cambridge University Press (1998), pp. 1-29, [10.1017/CBO9780511551864.002](10.1017/CBO9780511551864.002)

12. Ryu D., Famiglietti J.S.
Multi-scale spatial correlation and scaling behavior of surface soil moisture
Geophys Res Lett, 33 (2006), p. L08404, [10.1029/2006GL025831](10.1029/2006GL025831)

13. Choi M., Jacobs J.M.
Spatial soil moisture scaling structure during Soil Moisture Experiment 2005
Hydrol Processes, 25 (2011), pp. 926-932, [10.1002/hyp.7877](10.1002/hyp.7877)

14. Gebremichael M., Rigon R., Bertoldi G., Over T.M.
On the scaling characteristics of observed and simulated spatial soil moisture fields
Nonlinear Processes Geophys, 16 (2009), pp. 141-150

15. Western A.W., Blöschl G.On the spatial scaling of soil moisture
J Hydrol, 217 (1999), pp. 203-224, [10.1016/S0022-1694(98)00232-7](10.1016/S0022-1694(98)00232-7)

16. Shin Y., Mohanty B.P.
Development of a deterministic downscaling algorithm for remote sensing soil moisture footprint using soil and vegetation classifications
Water Resour Res, 49 (2013), pp. 6208-6228, 10.1002/wrcr.20495

17. Ines A.V.M., Mohanty B.P., Shin Y.
An unmixing algorithm for remotely sensed soil moisture
Water Resour Res, 49 (2013), pp. 408-425, [10.1029/2012WR012379](10.1029/2012WR012379)

18. Busch F.A., Niemann J.D., Coleman M.
Evaluation of an empirical orthogonal function-based method to downscale soil moisture patterns based on topographical attributes
Hydrol Processes, 26 (2012), pp. 2696-2709, [10.1002/hyp.8363](10.1002/hyp.8363)

19. Kim G., Barros A.P.
Downscaling of remotely sensed soil moisture with a modified fractal interpolation method using contraction mapping and ancillary data
Remote Sens Environ, 83 (2002), pp. 400-413, [10.1016/S0034-4257(02)00044-5](10.1016/S0034-4257(02)00044-5)

20. Mascaro G., Vivoni E.R., Deidda R.
Downscaling soil moisture in the southern Great Plains through a calibrated multifractal model for land surface modeling applications
Water Resour Res, 46 (2010), pp. 1-18, [10.1029/2009WR008855](10.1029/2009WR008855)

21. Rodriguez-Iturbe I., Vogel G.K., Rigon R., Entekhabi D., Castelli F., Rinaldo A.
On the spatial organization of soil moisture fields
Geophys Res Lett, 22 (1995), pp. 2757-2760, [10.1029/95GL02779](10.1029/95GL02779)

22. Biswas A., Zeleke T.B., Si B.C.
Multifractal detrended fluctuation analysis in examining scaling properties of the spatial patterns of soil water storage
Nonlinear Processes Geophys, 19 (2012), pp. 227-238, [10.5194/npg-19-227-2012](10.5194/npg-19-227-2012)

23. Laguardia G., Di Domenico A., Gebremichael M.
On the critical behaviour of observed and simulated spatial soil moisture fields during SGP97
Remote Sens, 2 (2010), pp. 2097-2110, [10.3390/rs2092097](10.3390/rs2092097)

24. Di Domenico A., Laguardia G., Fiorentino M.
Capturing critical behaviour in soil moisture spatio-temporal dynamics
Adv Water Resour, 30 (2007), pp. 543-554, 10.1016/j.advwatres.2006.04.007
25. Mascaro G., Vivoni E.R., Deidda R.
Soil moisture downscaling across climate regions and its emergent properties
J Geophys Res, 116 (2011), pp. 1-19, 10.1029/2011JD016231
26. Syed T.H., Famiglietti J.S., Rodell M., Chen J., Wilson C.R.
Analysis of terrestrial water storage changes from GRACE and GLDAS
Water Resour Res, 44 (2008), p. W02433, 10.1029/2006WR005779
27. Hu Z., Islam S., Cheng Y.
Statistical characterization of remotely sensed soil moisture images
Remote Sens Environ, 61 (1997), pp. 310-318, 10.1016/S0034-4257(97)89498-9
28. Pelletier J.D., Malamud B.D., Blodgett T., Turcotte D.L.
Scale-invariance of soil moisture variability and its implications for the frequency-size distribution of landslides
Eng Geol, 48 (1997), pp. 255-268, 10.1016/S0013-7952(97)00041-0
29. Di Domenico A., Laguardia G.
On the relations between critical behaviour of soil moisture spatio-temporal dynamics and catchment descriptors
CATENA, 86 (2011), pp. 49-56, 10.1016/j.catena.2011.02.001
30. Manfreda S., McCabe M.F., Fiorentino M., Rodríguez-Iturbe I., Wood E.F.
Scaling characteristics of spatial patterns of soil moisture from distributed modelling
Adv Water Resour, 30 (2007), pp. 2145-2150, 10.1016/j.advwatres.2006.07.009
31. Kumar P.A multiple scale state-space model for characterizing subgrid scale variability of near-surface soil moisture
IEEE Trans Geosci Remote Sens, 37 (1999), pp. 182-197, 10.1109/36.739153
32. Beven K.
Linking parameters across scales: subgrid parameterizations and scale dependent hydrological models
Hydrol Processes, 9 (1995), pp. 507-525, 10.1002/hyp.3360090504
33. Bloschl G., Sivapalan M.
Scale issues in hydrological modelling: a review
Hydrol Processes, 9 (1995), pp. 251-290
34. Beven K.
A manifesto for the equifinality thesis
J Hydrol, 320 (2006), pp. 18-36, 10.1016/j.jhydrol.2005.07.007
35. Arrigo J.A.S., Salvucci G.D.
Investigation hydrologic scaling: observed effects of heterogeneity and nonlocal processes across hillslope, watershed, and regional scales
Water Resour Res, 41 (2005), p. W11417, 10.1029/2005WR004032
36. Nykanen D.K., Foufoula-Georgiou E.
Soil moisture variability and scale-dependency of nonlinear parameterizations in coupled land- atmosphere models
Adv Water Resour, 24 (2001), pp. 1143-1157, 10.1016/S0309-1708(01)00046-X
37. Wood E.F.
Effects of soil moisture aggregation on surface evaporative fluxes
J Hydrol, 190 (1997), pp. 397-412, 10.1016/S0022-1694(96)03135-6
38. Vivoni E.R., Entekhabi D., Bras R.L., Ivanov V.Y.
Controls on runoff generation and scale-dependence in a distributed hydrologic model
Hydrol Earth Syst Sci, 11 (2007), pp. 1683-1701, 10.5194/hess-11-1683-2007
39. Perrier E.M.A., Bird N.R.A.
The PSF model of soil structure: a multiscale approach
Pachepsky Y., Radcliffe D.E., Selim H.M. (Eds.),
Scaling methods soil physics (2003)

40. Shen C., Phanikumar M.S.
An efficient space-fractional dispersion approximation for stream solute transport modeling
Adv Water Resour, 32 (2009), pp. 1482-1494, 10.1016/j.advwatres.2009.07.001

41. Benson D.A., Meerschaert M.M., Revielle J.
Fractional calculus in hydrologic modeling: a numerical perspective
Adv Water Resour, 51 (2013), pp. 479-497, 10.1016/j.advwatres.2012.04.005

42. Nogueira M., Barros A.P., Miranda P.M.A.
Multifractal properties of embedded convective structures in orographic precipitation: toward subgrid-scale predictability
Nonlinear Processes Geophys, 20 (2013), pp. 605-620, 10.5194/npg-20-605-2013

43. Dyskin A.V.
Continuum fractal mechanics of the earth's crust
Donnellan A., Mora P., Matsu'ura M., Yin X. (Eds.),
Computational earthquake science part I, Birkhäuser Basel, Basel (2004)

44. Chen Q., Gunzburger M., Ringler T.
A scale-invariant formulation of the anticipated potential vorticity method
Mon Weather Rev, 139 (2011), pp. 2614-2629, 10.1175/MWR-D-10-05004.1

45. W E., Yue X.Y.
Heterogeneous multiscale method for locally self-similar problems
Commun Math Sci, 2 (2004), pp. 137-144

46. Chorin A.J.
Averaging and renormalization for the Korteveg-deVries-Burgers equation
Proc Natl Acad Sci U S A, 100 (2003), pp. 9674-9679, 10.1073/pnas.1334126100

47. Shen C., Niu J., Phanikumar M.S.
Evaluating controls on coupled hydrologic and vegetation dynamics in a humid continental climate watershed using a subsurface–land surface processes model
Water Resour Res, 49 (2013), pp. 2552-2572, 10.1002/wrcr.20189

48. Ivanov V.Y., Fatichi S., Jenerette G.D., Espeleta J.F., Troch P.A., Huxman T.E.
Hysteresis of soil moisture spatial heterogeneity and the "homogenizing" effect of vegetation
Water Resour Res, 46 (2010), pp. 1-15, 10.1029/2009WR008611

49. Schaefli B., Harman C.J., Sivapalan M., Schymanski S.J.
HESS Opinions: hydrologic predictions in a changing environment: behavioral modeling
Hydrol Earth Syst Sci, 15 (2011), pp. 635-646, 10.5194/hess-15-635-2011

50. Sivapalan M., Thompson S.E., Harman C.J., Basu N.B., Kumar P.
Water cycle dynamics in a changing environment: Improving predictability through synthesis
Water Resour Res, 47 (2011), pp. 1-7, 10.1029/2011WR011377

51. Thompson S.E., Harman C.J., Troch P.A., Brooks P.D., Sivapalan M.
Spatial scale dependence of ecohydrologically mediated water balance partitioning: a synthesis framework for catchment ecohydrology
Water Resour Res, 47 (2011), p. W00J03, 10.1029/2010WR009998

52. Vivoni E.R.
Spatial patterns, processes and predictions in ecohydrology: integrating technologies to meet the challenge
Ecohydrology, 5 (2012), pp. 235-241, 10.1002/eco.1248

53. Wagener T., Sivapalan M., Troch P.A., McGlynn B.L., Harman C.J., Gupta H.V., et al.
The future of hydrology: An evolving science for a changing world
Water Resour Res, 46 (2010), pp. 1-10, 10.1029/2009WR008906

54. Deidda R.
Multifractal analysis and simulation of rainfall fields in space
Phys Chem Earth, Part B Hydrol Oceans Atmos, 24 (1999), pp. 73-78, 10.1016/S1464-1909(98)00014-8

55. Shen C., Phanikumar M.S.
A process-based, distributed hydrologic model based on a large-scale method for surface–subsurface coupling
Adv Water Resour, 33 (2010), pp. 1524-1541, 10.1016/j.advwatres.2010.09.002

56. Shen C., Niu J., Fang K.

Quantifying the effects of data integration algorithms on the outcomes of a subsurface–land surface processes model
Environ Modell Software, 59 (2014), pp. 146-161, 10.1016/j.envsoft.2014.05.006

57. Lawrence D.M., Oleson K.W., Flanner M.G., Thornton P.E., Swenson S.C., Lawrence P.J., et al.
Parameterization improvements and functional and structural advances in Version 4 of the Community Land Model 2011. http://dx.doi.org/10.1029/2011MS000045.

58. Oleson K., Lawrence D.M., Bonan G.B., Flanner M., Kluzek E., Lawrence P., et al.
Technical description of version 4.0 of the Community Land Model (CLM). NCAR Technical note, NCAR/TN-478+STR; 2010.

59. Koven C.D., Riley W.J., Subin Z.M., Tang J.Y., Torn M.S., Collins W.D., et al.
The effect of vertically resolved soil biogeochemistry and alternate soil C and N models on C dynamics of CLM4
Biogeosciences, 10 (2013), pp. 7109-7131, 10.5194/bg-10-7109-2013

60. Tang J.Y., Riley W.J., Koven C.D., Subin Z.M.
CLM4-BeTR, a generic biogeochemical transport and reaction module for CLM4: model development, evaluation, and application
Geosci Model Dev, 6 (2013), pp. 127-140, 10.5194/gmd-6-127-2013

61. Niu J., Shen C., Li S.-G., Phanikumar M.S.
Quantifying storage changes in regional Great Lakes watersheds using a coupled subsurface-land surface process model and GRACE, MODIS products
Water Resour Res, 50 (2014), pp. 7359-7377, 10.1002/2014WR015589

62. JPL
GRACE monthly mass grids – land
Jet Propuls Lab GRACE Tellus (2014)
Data Process by Sean Swenson

63. Gaur N., Mohanty B.P.
Evolution of physical controls for soil moisture in humid and subhumid watersheds
Water Resour Res, 49 (2013), pp. 1244-1258, 10.1002/wrcr.20069

64. Ryu D., Famiglietti J.S.Characterization of footprint-scale surface soil moisture variability using Gaussian and beta distribution functions during the Southern Great Plains 1997 (SGP97) hydrology experiment
Water Resour Res, 41 (2005), p. W12433, 10.1029/2004WR003835

65. MDNR
IFMAP/GAP Lower Peninsula Land Cover
Michigan Dep Nat Resour (2010)

66. NRCS. SSURGO Soil Survey Geographic Database. Nat Resour Conserv Serv 2010.

67. Schaap M.G., Leij F.J., van Genuchten M.T.
Rosetta: a computer program for estimating soil hydraulic parameters with hierarchical pedotransfer functions
J Hydrol, 251 (2001), pp. 163-176, 10.1016/S0022-1694(01)00466-8

68. GWIM. State of Michigan Public Act 148 Groundwater Inventory and Mapping Project (GWIM). Technical report 2010.

69. Oztan M., Li S.G.
GIS-enabled modeling of Michigan's groundwater systems
Michigan State University (2011)

70. Simard A., Li S.
Predicting groundwater flow and transport using Michigan's statewide wellogic database
Michigan State University (2007)

71. Shen C., Niu J., Phanikumar M.
Evaluating controls on coupled hydrologic and vegetation dynamics in a humid continental climate watershed using a subsurface-land surface processes model
Water Resour Res, 49 (2013), pp. 2552-2572, 10.1002/wrcr.20189

72. Rosenbaum U., Bogena H.R., Herbst M., Huisman J.A., Peterson T.J., Weuthen A., et al.
Seasonal and event dynamics of spatial soil moisture patterns at the small catchment scale
Water Resour Res, 48 (2012), p. W10544, 10.1029/2011WR011518

73. Vivoni E.R., Rodríguez J.C., Watts C.J.
    On the spatiotemporal variability of soil moisture and evapotranspiration in a mountainous basin within the North American monsoon region
    Water Resour Res, 46 (2010), p. W02509, [10.1029/2009WR008240](10.1029/2009WR008240)
74. Peters-Lidard C., Pan F., Wood E.
    A re-examination of modeled and measured soil moisture spatial variability and its implications for land surface modeling
    Adv Water Resour, 24 (2001), pp. 1069-1083, [10.1016/S0309-1708(01)00035-5](10.1016/S0309-1708(01)00035-5)
75. Thompson S.E., Harman C.J., Schumer R., Wilson J.S., Basu N.B., Brooks P.D., et al.
    Patterns, puzzles and people: implementing hydrologic synthesis
    Hydrol Processes, 25 (2011), pp. 3256-3266, [10.1002/hyp.8234](10.1002/hyp.8234)
76. Huber P.J.Robust statistics
    John Wiley & Sons, Inc., Hoboken, NJ, USA (1981)